

2008

Wing mechanization design and analysis for a perching micro air vehicle

Jennifer Marie Lukens
University of Dayton

Follow this and additional works at: https://ecommons.udayton.edu/graduate_theses

Recommended Citation

Lukens, Jennifer Marie, "Wing mechanization design and analysis for a perching micro air vehicle" (2008).
Graduate Theses and Dissertations. 4084.
https://ecommons.udayton.edu/graduate_theses/4084

This Thesis is brought to you for free and open access by the Theses and Dissertations at eCommons. It has been accepted for inclusion in Graduate Theses and Dissertations by an authorized administrator of eCommons. For more information, please contact mschlangen1@udayton.edu, ecommons@udayton.edu.

**Wing Mechanization Design and Analysis for a Perching
Micro Air Vehicle**

Thesis

Submitted to

The School of Engineering of the
UNIVERSITY OF DAYTON

in Partial Fulfillment of the Requirements for

The Degree

Master of Science in Aerospace Engineering

by

Jennifer Marie Lukens

UNIVERSITY OF DAYTON

Dayton, Ohio

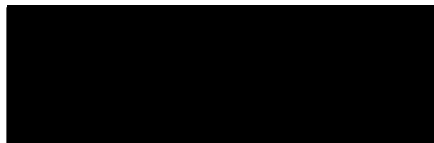
May, 2008

Wing Mechanization Design and Analysis for a Perching Micro Air Vehicle

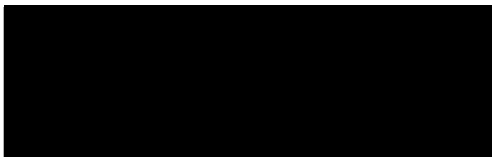
APPROVED BY:



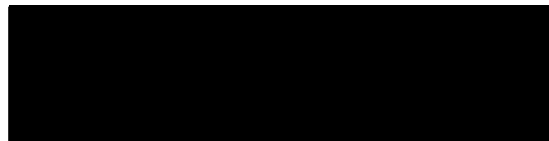
Brian Sanders, Ph.D.
Advisory Committee Chairman
Adjunct Professor, Mechanical and
Aerospace Engineering Department



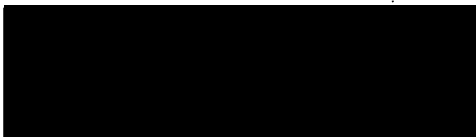
Kevin Hallinan, Ph.D.
Committee Member
Chair, Mechanical and Aerospace
Engineering Department



Greg Reich, Ph.D.
Committee Member
Senior Aerospace Engineer
Air Force Research Laboratory



Malcolm W. Daniels, Ph.D.
Associate Dean
School of Engineering



Joseph E. Saliba, Ph.D., P.E.
Dean, School of Engineering

ABSTRACT

Wing Mechanization Design and Analysis for a Perching Micro Air Vehicle

Name: Lukens, Jennifer Marie

University of Dayton, 2008

Advisor: Brian Sanders, Ph.D.

Interest in the design and development of bird-like micro air vehicles (MAVs) for sensory applications has emerged in recent years. This project is an investigation of how a bird-like MAV could be mechanized to land with approximately zero vertical and horizontal velocity, inspired by a bird perching maneuver. The objective of this research project is to determine the degrees of freedom and motions necessary to complete this landing maneuver and to develop a mechanized model to perform the required motion while still meeting size, weight, and power requirements of a notional vehicle to perform the maneuver. This thesis focuses on the wing mechanization design and kinematic mechanism making the wing motion possible as well as the structure/mechanism integration. A mechanized wing concept for a perching micro air vehicle has been designed and manufactured with wings capable of rotating at two spanwise joints to simulate the rotational motion of a bird's wings during a perching maneuver. The final design met all size, weight, and power requirements. Wind tunnel testing and analytical simulation was also completed to further develop the model and to determine order of magnitude loads acting on the vehicle during a typical perching maneuver. The model developed is a successful first iteration vehicle that incorporates multiple degrees of freedom in the wings to facilitate perching.

Acknowledgements

First, I would like to thank my family and my fiancé, Eric Fries, for their loving support. I would also like to thank Brian Sanders, Greg Reich, and Jason Bowman for assisting me with my thesis research and for this opportunity. I would like to thank Leon Chuck, Phil Doecker, and Michael Turner at the University of Dayton for their technical advice. I would like to thank Aaron Altman for the opportunity to utilize the wind tunnel under his direction, for his insightful suggestions, and for being a wonderful advisor throughout my college career. I would like to thank Ward Engineering for fabricating my wind tunnel model and for their technical support in the detailed design of the MAV model. Thanks to UDRI, especially Geoff Frank, for their support in the prototype labs. And last, but not least, to Kevin Hallinan for his advice, support, and help throughout college and for always having faith in me.

Contents

Chapter

1	Introduction	1
1.1	Motivation	1
1.2	Micro Air Vehicle Applications	2
1.3	Biological Inspiration	3
1.3.1	Perching	4
1.4	Problem Statement	5
2	Background	8
2.1	Micro Air Vehicle Designs	8
2.1.1	Fixed-Wing Vehicles	10
2.1.2	Ornithopter Development	11
2.1.3	Biological Inspiration for Aircraft Design	13
2.2	Avian Flight	15
2.2.1	Bones and Joints	16
2.2.2	Muscles	16
2.2.3	Perching	18
2.3	Summary	21

3	Model Design	22
3.1	Design Concept	22
3.2	Fuselage	24
3.3	Wings	25
3.3.1	Flight Modes	27
3.3.2	Wing Loads	28
3.3.3	Spar	31
3.3.4	Mechanization	36
3.4	Fabrication	39
4	Experimental Testing	41
4.1	Wind Tunnel Test	41
4.1.1	Tunnel Description	41
4.1.2	Force Transducer	42
4.1.3	Test Setup	45
4.1.4	Test Procedure	47
4.1.5	Results	49
4.2	Power Requirements	65
4.2.1	Circuit	65
4.2.2	Benchtop Test Setup	66
4.2.3	Results	69
4.2.4	Energy Requirements	71
5	Analytical Model	77
5.0.5	Analysis Tool	77
5.0.6	Simulation Model	78
5.0.7	Results	81

5.0.8 Comparison to Wind Tunnel Results	88
6 Conclusions and Recommendations	91
6.1 Conclusions	91
6.2 Recommendations	92
6.3 Summary	93
 Appendix	
A Mount Design	94
B Calibration Curves	100
C Wind Tunnel Results	104
D Analysis Results	110
 Bibliography	113

Figures

Figure

1.1 Bird Body and Wing Incidence at Landing [1]	6
2.1 Two MAVs a.)Fixed Wing MAV: The Black Widow b.)Flapping Wing MAV: Microbat [2]	9
2.2 Two Fixed Wing MAV's a.)MLB's Trochoid b.)University of Florida's Flexible Wing Design [3]	10
2.3 The GENMAV [4]	11
2.4 Berkeley's Robofly [3]	12
2.5 The University of Florida's Gull-Wing Morphing Vehicle [5]	14
2.6 The University of Florida's Variable Sweep Vehicle [6]	14
2.7 Typical Bird Wing Joints	17
2.8 Bird Wing Bones	17
2.9 Bird-Like Landing Trajectory	20
3.1 Mechanized Model Configuration-Head on View	23
3.2 Model at Two Different Configurations a.)Distal Sections at 10 Degrees and Proximal Sections at 45 Degrees b.)Entire Wing at 90 Degrees	26
3.3 NACA 0009 Airfoil Dimensions	27
3.4 Lift Coefficient for Angles of Attack up to 180 Degrees [7]	29

3.5 Drag Coefficient for Angles of Attack up to 180 Degrees [7]	29
3.6 Lift Distribution (Wing Panels at 10 Degrees, Speed 10 m/s)	32
3.7 Bending Moment (Wing Panels at 10 Degrees, Speed 10 m/s)	32
3.8 Coaxial Cylindrical Spar Design	33
3.9 Maximum Shearing Stress for Three Generic Moment Coefficients	35
3.10 Maximum Bending Stress for Three Wing Incidence Angles	37
3.11 Model Actuation	38
3.12 Control Panel	39
4.1 Nano43 Force Transducer	42
4.2 Calibration Setup	44
4.3 Wind Tunnel Experimental Setup	46
4.4 Model Position in Wind Tunnel	48
4.5 Wing Incidence Measurement	48
4.6 Comparison of Raw Verses Filtered Data: a)Raw Data for Test 22 b)Filtered Data for Test 22	51
4.7 Comparison of a) 1 m/s to b) 5 m/s Test	55
4.8 Lift and Drag for Test 15, 5 m/s	57
4.9 Lift and Drag for Test 20, 7.5 m/s	58
4.10 Lift and Drag for Test 22, 7.5 m/s	59
4.11 Lift and Drag for Test 29, 5 m/s	60
4.12 Power Measurement Circuit	67
4.13 Y-Harness	67
4.14 Benchtop Power Test Setup	68
4.15 Power Results for Proximal Wing Rotation from 0 to 85 Degrees	70
4.16 Power: Rotation of Proximal Wing From 0 Degrees to 10 Degrees	73

4.17 Power: Rotation of Proximal Wing From 0 Degrees to 45 Degrees	74
4.18 Power: Rotation of Proximal Wing From 10 Degrees to 0 Degrees	74
4.19 Power: Rotation of Proximal Wing From 45 Degrees to 0 Degrees	75
4.20 Power: Rotation of Proximal Wing From 85 Degrees to 0 Degrees	75
5.1 Lift and Drag Coefficient Splines	78
5.2 Analytical Model in ADAMS	79
5.3 Analytical Model in ADAMS With Proximal Wing Sections at 82 Degrees and Distal Wing Sections at 6 Degrees.	81
5.4 Analytical Lift, Drag, and Pitching Moment Results for Test 17	83
5.5 Analytical Lift, Drag, and Pitching Moment Results for Test 22	83
5.6 Analytical Lift, Drag, and Pitching Moment Results for Test 25	84
5.7 Analytical Lift, Drag, and Pitching Moment Results for Test 29	85
5.8 Analytical Lift, Drag, and Pitching Moment Results for Full Wing Rotation from 0 to 25 Degrees at 10 m/s	86
5.9 Possible Perching Trajectories	89
5.10 Comparison of Wind Tunnel and Analytical Results for Test 29 a.)Analytical Model Results b.)Wind Tunnel Results	89
5.11 Comparison of Wind Tunnel and Analytical Results for Test 22 a.)Analytical Model Results b.)Wind Tunnel Results	90
A.1 Mount Plate	95
A.2 Sting	96
A.3 Base Plate	97
A.4 Mount Assembly: Two Views	98
A.5 Calibration Plate	99

B.1	Calibration Curves: Lift	100
B.2	Calibration Curves: Drag	101
B.3	Calibration Curves: Side Force	101
B.4	Calibration Curves: Positive Pitching Moment	101
B.5	Calibration Curves: Negative Pitching Moment	102
B.6	Calibration Curves: Positive Rolling Moment	102
B.7	Calibration Curves: Negative Rolling Moment	102
B.8	Calibration Curves: Positive Yawing Moment	103
B.9	Calibration Curves: Negative Yawing Moment	103
C.1	Lift and Drag for Test 17	105
C.2	Lift and Drag for Test 25	106
C.3	Lift and Drag for Test 28	107
C.4	Lift and Drag for Test 32	108
D.1	Analytical Lift, Drag, and Pitching Moment Results for Test 15	111
D.2	Analytical Lift, Drag, and Pitching Moment Results for Test 20	111
D.3	Analytical Lift, Drag, and Pitching Moment Results for Test 28	112

Tables

Table

3.1	Cases Analyzed for Load Calculations	30
3.2	Model Weight Breakdown	40
4.1	Specifications for Nano43	43
4.2	Actual Calibration for Nano43	44
4.3	Metric Calibration for Nano43	44
4.4	Wind Tunnel Test Matrix	50
4.5	Wall Interference Corrections	54
4.6	Wind Tunnel Test Details	56
4.7	Power Test Results	72
4.8	Power Test Results- Averages	73

Chapter 1

Introduction

1.1 Motivation

Interest in the design and development of bird-like micro air vehicles has emerged in recent years due to the myriad of applications possible for such a vehicle. Micro air vehicles (MAVs) are characterized by their low flight speed, small size, and low Reynolds number. The definition of MAVs is somewhat arbitrary; however, the MAV designed in this project has a wingspan of 61 cm, mass of 306 g and cruise speed of 10 m/s. These small aircraft have the potential to be valuable assets for many organizations, especially for use in military operations. One possible mission scenario for a MAV is to travel into dangerous territory covertly, land on a branch, ledge, or rooftop, collect data and transmit it to a remote source. This application alone could potentially save the lives of soldiers and provide extensive sensory data previously inaccessible. Micro air vehicles do; however, offer many challenges that require the integration of several cutting edge technologies. Although there have been several successful small scale vehicles developed, there are many advances in this field that need to be made before a MAV can be successful in these types of missions. Creating a MAV that acts and looks similar to a bird allows the vehicle to be "hidden in plain sight," meaning that the vehicle would blend in with, or not stand out from, its surrounding environment, improving its ability for the above mentioned sensory missions. Inspiration from birds and insects does not only provide an advanced disguise

for the vehicle, but it helps answer some of the most difficult questions about small vehicle development. Research to date in the area of bird-like MAV development has focused strongly on the aerodynamics of flapping and on the kinematic mechanism that makes the beating motion possible. One thing missing is an investigation of how a bird-like MAV could be mechanized to land with a trajectory similar to a bird perching motion. This landing maneuver is essential to the success of micro air vehicles. To date, most MAV's have a very short endurance making their mission capabilities significantly reduced. Creating a vehicle that can perch on an object not only allows the vehicle to monitor a situation and transmit data, but also provides the opportunity to recharge its energy source, possibly by the use of energy harvesting techniques.

1.2 Micro Air Vehicle Applications

Uninhabited air vehicles (UAVs) have emerged as the chosen vehicle platform for many sensory and surveillance missions in hostile environments usually too dangerous for manned vehicles [8, 9, 10]. Several UAVs such as the Global Hawk and Predator have been very successful in many missions. Shrinking the size of conventional UAVs results in a new class of vehicles. Micro air vehicles are unmanned vehicles of small size (under 1 m wingspan) capable of a variety of missions, and are especially ideal for reconnaissance operations because of their low radar cross sections and low noise [11]. Other possible MAV missions include surveillance, detection, communication, sensor placements for information in hostage recovery and counter drug operations, as well as sensing operations to detect biological agents, chemical compounds, and nuclear materials. MAVs are especially suited to perform in urban environments and interior operations where large scale vehicles are not capable of infiltrating. Often many of these missions include a necessity for remote sensing, communication, payload delivery, and rescue capabilities, but because of

their small size, creating a MAV with these capabilities proves to be difficult [4]. The myriad of possible missions and challenging obstacles to be overcome has recently made MAV development the top focus of many research groups, yet there remain many opportunities to improve current MAV designs and develop new vehicle concepts.

1.3 Biological Inspiration

Micro air vehicle development faces several design challenges specific to the vehicle category. One of these issues involves the low Reynolds number regime, on the order of 5×10^4 to 2×10^5 , that the vehicle operates in, which results in complex flows during flight [8, 11, 12, 13, 14]. The highly viscous laminar flow physics present at low Reynolds numbers results in unexpected airfoil performance and other complex issues not usually associated with conventional, large scale, aircraft. To help understand the complex flow phenomena associated with low Reynolds number flight, birds and insects are often studied. Nature has provided flyers that are capable of very efficient flight in low Reynolds number regimes and demonstrate it with grace [8]. Inspiration from Nature's flyers provides a starting point for developing efficient and graceful aircraft. Birds are living highly advanced morphing systems capable of extreme maneuvers desirable for many aircraft applications. Their ability to morph their wings allows for the expansion of the typical flight envelope of MAVs. Shape variations that birds can control include changes in: anhedral, dihedral, planform, camber, aspect ratio, wing sweep, wing warping, and wing incidence among others [8]. Simple mechanical equivalents to the structure of bird wings could allow MAVs to mimic bird motion by adapting their wings to an optimal shape to increase efficiency for specific flight tasks [15]. This type of morphing can be developed to optimize steep descent, minimum radius turns, loitering, sensor pointing, and other tasks. Developing a structure that incorporates the degrees of freedom in birds wings can enhance

the MAV's operation, especially in urban environments, by allowing the vehicle to mimic the refined and efficient motions birds utilize for flight. Besides increasing maneuverability and efficiency, mimicking bird wing motion also aids in reconnaissance and stealth. The more bird-like a MAV is, the more likely that it will remain unnoticed in its environment. Biomimicry, in this sense, can allow the MAV to be hidden in plain sight to further increase its capability to perform a variety of missions. Because birds are superior to current aircraft, the logical next step in aircraft design is to learn from avian flight and to use bird inspired morphing techniques to improve the next generation of aircraft.

1.3.1 Perching

Due to their lack of ability to carry large power sources, many MAV's often need to return to their base to be recharged. Increasing endurance or range would significantly improve the mission capabilities of MAV's. Instead of increasing the vehicle's endurance by incorporating a larger energy source, another way to allow a vehicle to collect and transmit data for a long period of time, extend the time in the field, and increase the range of the vehicle, is to design the MAV to perch on an existing object. While perched, the vehicle could recharge its power supplies using energy harvesting techniques and eventually continue its mission without returning to its base [16]. While recharging, the vehicle could communicate data with a remote source. In order for this scenario to be practical, the vehicle must be able to land on an object suited for recharging such as a branch, ledge or similar object.

Landing and retrieval has been an underling issue for MAV development. To date there have been many attempts at developing systems for retrieving fixed wing MAVs which include using a deep stall approach, a catching net, mounted hooks, and parachutes [17]. Instead of this type of assisted retrieval, the main focus of this project is to develop a vehicle that is capable of perching, or landing on a point in space with nominal vertical and

horizontal velocity. To date, very few studies have been completed that research how to land the MAV on a small surface.

For conventional landing on a runway, a vehicle is brought to nearly zero vertical velocity, but with a significant horizontal velocity. Friction in the wheels and further braking techniques allow the vehicle to come to a stop after it has touched the ground. In the proposed scenario, the vehicle will land on a point in space without a runway. Perching, in this sense, uses aerodynamics for landing rather than friction or heavy thrust vectoring systems to achieve the maneuver. Perching often uses a high body angle and wing incidence approach seen in Figure 1.1 and uses drag from air flow to reduce horizontal velocity. This project focuses on determining the required wing degrees of freedom for this maneuver and focuses specifically on the effects of high body/wing rotation.

1.4 Problem Statement

The development of micro air vehicles has been led by the Department of Defense to create light weight, small vehicles capable of a variety of missions including sensory missions over land as well as in confined spaces such as tunnels or in urban environments between buildings [8]. The requirement for these missions has led to the additional desired capability of a vehicle able to perch on buildings to provide situation awareness and allow the vehicle to recharge [8]. The ultimate goal of this research project is to create a MAV that can perch without utilizing flapping. To achieve this, the necessary degrees of freedom to complete this maneuver were determined by researching bird-like motions and by studying the effects of wing rotational motion through high wing incidence. The model developed in the project is a first iteration at integrating actuators into the wings for perching mechanization, and considers not only the geometric and weight requirements, but also the power necessary to perform this type of maneuver. Additional degrees of freedom in

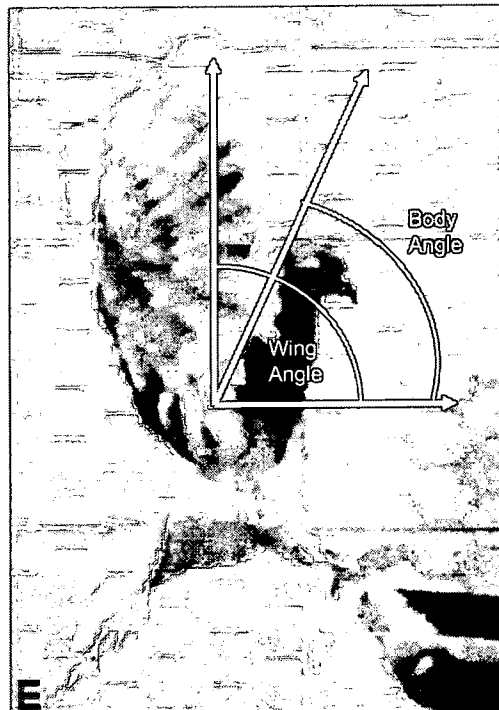


Figure 1.1: Bird Body and Wing Incidence at Landing [1]

the wing, tail, and body may need to be investigated to more accurately mimic bird motion during perching.

Chapter 2

Background

This chapter will explore current micro air vehicle technology and how biological inspiration has affected growth in this area. Avian flight modes, bones, joints, and muscles will be discussed as they provide implications for MAV structural design and degrees of freedom required for a perched landing. Finally, the project goals will be addressed and the remainder of the thesis will be outlined.

2.1 Micro Air Vehicle Designs

Increased interest in the design of MAVs has led to the development of many micro air vehicle concepts. There have been three basic classes of MAV designs developed: fixed wing, rotary wing, and flapping wing vehicles. Since this project focuses on utilizing biological inspiration for aircraft design and because rotary wing vehicles do not imitate birds or insects, this type of vehicle has not been focused on in this project. Instead, only the fixed and flapping wing vehicles are discussed.

Two successful MAVs developed in these categories are the Black Widow, a fixed wing aircraft, and Microbat, a flapping wing vehicle, both shown in Figure 2.1. The Black Widow, developed by AeroVironment Incorporated, is a 15.24 cm span aircraft capable of around a 30 minute endurance with a 2 km range at only 80 grams including a video camera payload capable of delivering real-time video imagery to a remote operator. Low

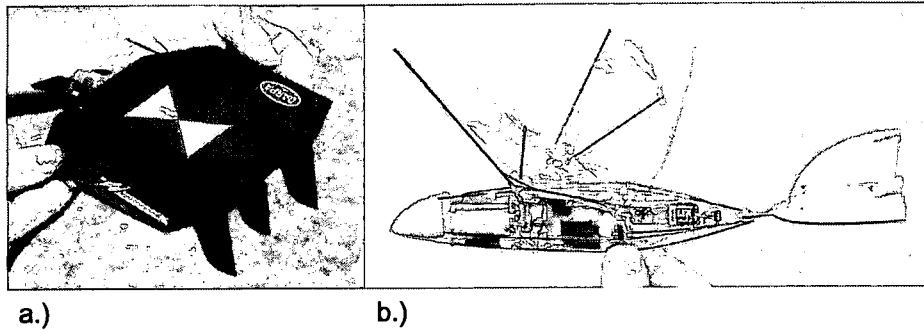


Figure 2.1: Two MAVs a.)Fixed Wing MAV: The Black Widow b.)Flapping Wing MAV: Microbat [2]

aspect ratio wing designs, as found on the Black Widow, are often seen on fixed wing micro air vehicles. At low Reynolds numbers wings with aspect ratios lower than 1.5 can be considered to have two forms of lift, linear and nonlinear. The nonlinear lift is created by low-pressure cells on the wing's top surface created by tip vortices which increases the lift-curve slope as angle of attack increases. This results in a high stall angle [14]. The Black Widow has surprisingly good performance capabilities for its size and vehicle class. Its 30 minute endurance and ability to carry a camera makes it one of the most practical MAVs developed to date. However, even with a 2 km range, the vehicle is not capable of performing some of the missions desired of MAVs.

The Microbat is another impressive vehicle. This small ornithopter, flapping wing vehicle, was developed jointly by the California Institute of Technology, UCLA, and AeroVironment Inc. and is capable of a 31 minute endurance with a 23 cm wingspan [2]. The Microbat was developed using historical ornithopter designs, wind tunnel tests, and flight test results. Several models of Microbat were constructed, and the design evolved with each iteration. This vehicle does not carry any onboard communication devices other than the radio used for remote control. Although the Microbat needs some improvements to be capable of the desired missions, this model made a great step in the direction of bio-

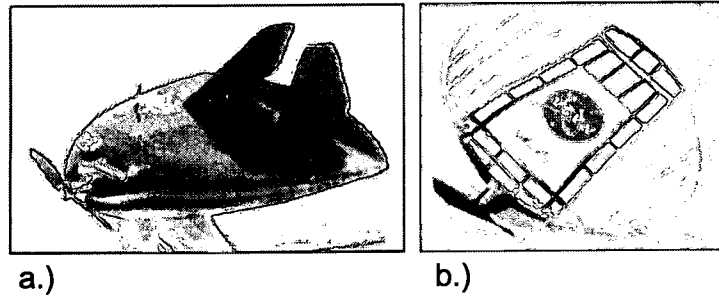


Figure 2.2: Two Fixed Wing MAV's a.)MLB's Trochoid b.)University of Florida's Flexible Wing Design [3]

inspired vehicles. These two vehicles demonstrate strong examples of the progress to date in MAV development.

2.1.1 Fixed-Wing Vehicles

Besides AeroVironment's Black Widow, many other fixed-wing vehicles have been developed. Radio Controlled (RC) aircraft are one type of fixed-wing aircraft and are available in hobby shops for recreation. However, slightly smaller models with more advanced flight control systems are desired. Some examples of successful fixed wing micro air vehicles include Steve Morris of MLB Co.'s Trochoid and the University of Florida's flexible wing design shown in Figure 2.2 [3]. The University of Florida's design incorporates a unique flexible structure inspired by sail technology and bat wing membranes. These fixed-wing vehicles, along with many others, perform well, but the designs do not incorporate the notion of biological inspiration in the visual sense.

To aid in the development of fixed-wing vehicles, the Air Force Research Laboratory has conducted significant MAV research for vehicles on the scale of 1-3 ft and has developed a 24 inch wingspan generic aircraft, the GENMAV, shown in Figure 2.3. This generic MAV was developed to serve as a reference for future MAV research and a basis for MAV

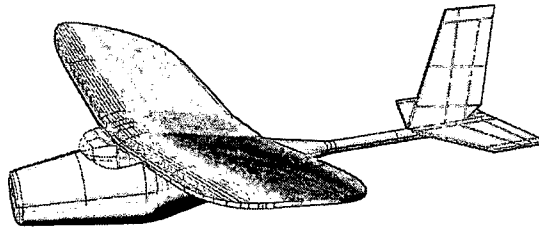


Figure 2.3: The GENMAV [4]

design [4]. By building off of the GENMAV design, researchers can complete somewhat controlled modifications to the vehicle to determine the effects of these changes. Research continues to grow in the development of fixed-wing vehicles; however, more interesting to this project is the growth and development of biologically inspired, flapping vehicles.

2.1.2 Ornithopter Development

Many micro air vehicle concepts have been developed that utilize flapping for lift and propulsion. These vehicles, known as ornithopters, attempt to mimic the flapping motion of birds and insects to generate lift and thrust required for flight. Flapping micro air vehicles have been studied by many groups resulting in the creation of several models such as AeroVironment's Microbat, and the University of California, Berkeley's fruitfly Robofly shown in Figure 2.4 [8, 3]. Robofly is one vehicle in a series of engineering projects developed by Berkeley to help understand insect flight mechanisms to emulate their behavior. Flapping flight is a complex topic that if mastered could lead to very efficient and practical vehicles.

Much other research has been completed that specifically studies flapping and the mechanisms required to create that movement. Madangopal et al. developed a biologically inspired design of a small flapping mechanism modeled off of an insect thorax that allows kinetic energy of the wing to be stored as elastic potential energy in the thorax during flap-

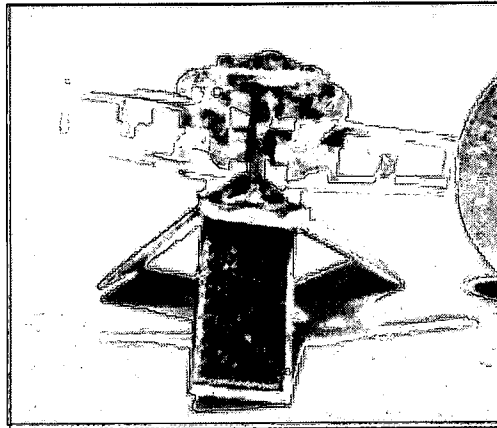


Figure 2.4: Berkeley's Robofly [3]

ping [18]. The stored energy pulls the wings down at the end of the upstroke aiding the motor and reducing the torque load. The reduced torque reduces the peak input power of the motor [18]. This project made a great leap in understanding the kinematics associated with flapping. Although the aerodynamics of flapping has been studied rigorously by aerodynamicists and biologists alike, the research has yet to culminate in a perching, fully functional flapping vehicle for sensory missions.

2.1.3 Biological Inspiration for Aircraft Design

The capabilities and performance of current MAVs are significantly less efficient and inferior in performance when compared to birds. By mimicking many of Nature's flyers, the performance of future MAVs could be improved.

Bird wings have several degrees of freedom which allow for graceful and efficient motion. Studying the benefits of including these degrees of freedom in MAV wings has led to the development of several vehicle concepts. Using inspiration from bird motion, Abdulrahim and Lind at the University of Florida studied the effects of an aircraft with gull-wing morphing capabilities in which the wings were able to change dihedral at the root and at a semispan joint with motion symmetric about the fuselage [5]. Two joints, with two degrees of freedom each, were used for each wing side [5, 15]. The different vehicle configurations are shown in Figure 2.5. Steep, slow airspeed dives performed by seagulls inspired the degree of freedom selection for this model. Including these joints in the wings broadened the flight envelope for the vehicle, making it capable of a variety of new maneuvers. Also from the University of Florida, Grand, Abdulrahim, and Lind studied the effects of multiple joint wing sweep on an aircraft [6]. The independent sweep configurations of this vehicle are shown in Figure 2.6. This vehicle was inspired by the ability of seagulls to roll and steeply dive. Again, the added degrees of freedom in the wing allowed for an expansion of the flight envelope. The research project described in this thesis uses the same design

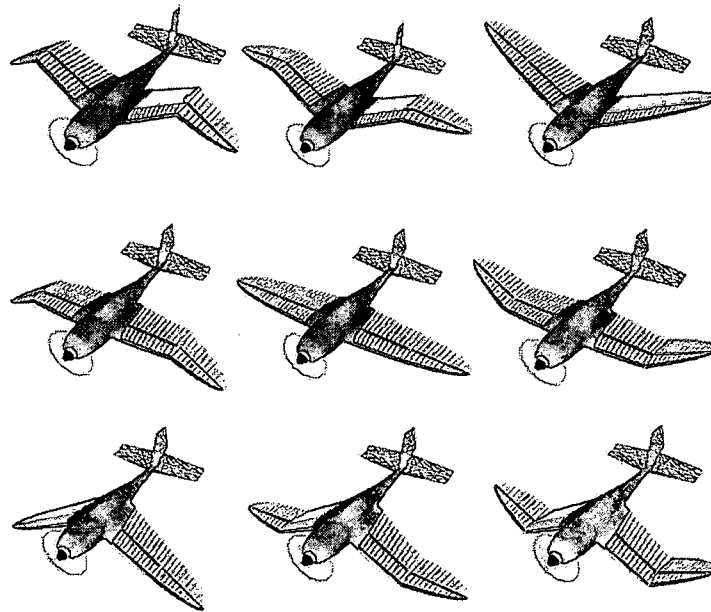


Figure 2.5: The University of Florida's Gull-Wing Morphing Vehicle [5]

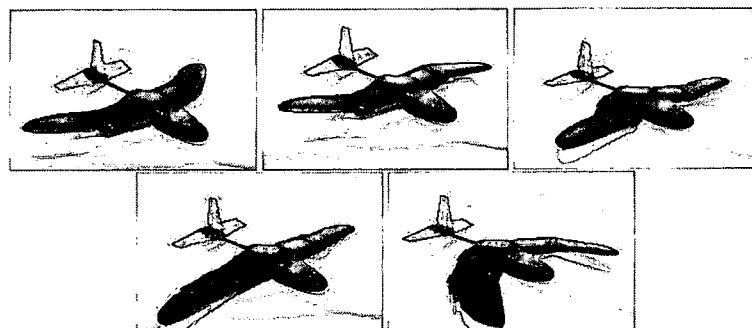


Figure 2.6: The University of Florida's Variable Sweep Vehicle [6]

idea to expand the flight envelope in hopes of incorporating degrees of freedom into the wings to allow for a perching maneuver.

There have been few other studies aimed at landing a MAV. Moschetta et al. investigated the possibility of developing a fixed wing MAV that exhibits hovering capabilities yet maintains a high cruise speed [19]. This project attempted to solve the problem of vertical take off and landing (VTOL) and hover for fixed wing MAVs by developing a tily-body model that rotates the body of the vehicle to sustain hover as well as a separate tilt-wing model that rotates the wings [19].

Wickenheiser et al. modeled an aircraft based off of the ARES Mars scout to complete a perching maneuver using aerodynamics only. This model is a blended-wing body with a folding tail boom with actuators incorporated into the tail degrees of freedom for perching [20]. This model makes a significant step toward completing a perching maneuver.

Multiple wing degrees of freedom for MAVs have been studied as mentioned above. What is missing is a study that incorporates a mechanized, multiple degree of freedom, vehicle designed specifically for perching with power requirements in mind. This project focuses on the development of a biologically inspired perching vehicle.

2.2 Avian Flight

Birds and insects are superior morphing systems that can be researched and examined to develop imitating vehicles. Extensive research has been completed by biologists on the physics of bird and insect flight. This research includes understanding the bones, feathers, and joints of birds as well as their muscles and flight capabilities. The information collected by biologists is important for developing a biologically inspired vehicle.

2.2.1 Bones and Joints

Bird wings are powerful, lightweight, musculo-skeletal structures. The wing bones only account for 6 percent of a bird's total mass [21]. A bird wing has three joints positioned similar to those in a human arm, these joints are the shoulder joint, elbow joint, and wrist joint shown in Figure 2.7. The shoulder joint is connected to the bird's rib cage at the wing root and allows for lateral and vertical motion, or sweep and dihedral change. A short bone, the humerus, connects the shoulder joint to the elbow joint, relatively close to the body, and allows for pure sweeping motion. Two parallel bones, the ulna and radius, connect the elbow joint to the wrist joint. The wrist joint moves in sweep and twist [15, 22]. These main wing bones, shown in Figure 2.8a, are very light, semi hollow circular cylinders. The hollow bones are supported by internal struts for added strength shown in Figure 2.8b. The lightweight structure of bird bones has implications toward material selection for MAV designs.

2.2.2 Muscles

The main flight muscle in birds, the pectoralis major, accounts for about 20 percent of a bird's mass [21, 23]. These muscles are responsible for providing the downstroke of the wings during flapping. When coupled with the pectoralis minor muscle, responsible for the upstroke, these two muscles make up from 25 to 35 percent of the bird's total mass. Information about these muscles has implications towards actuation requirements micro air vehicles need for sustainable flight.

Kenneth Dial measured the muscle intensity profiles from the three major shoulder muscles in rock doves during flapping flight to understand the purpose of the forelimb muscles [24]. He also completed tests to understand which muscles were utilized during different flight modes. After testing he proposed that the forelimb muscles were primarily

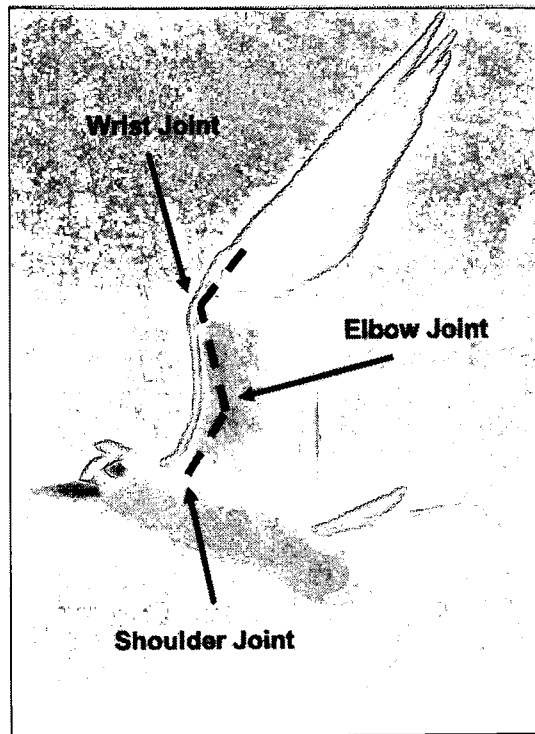


Figure 2.7: Typical Bird Wing Joints

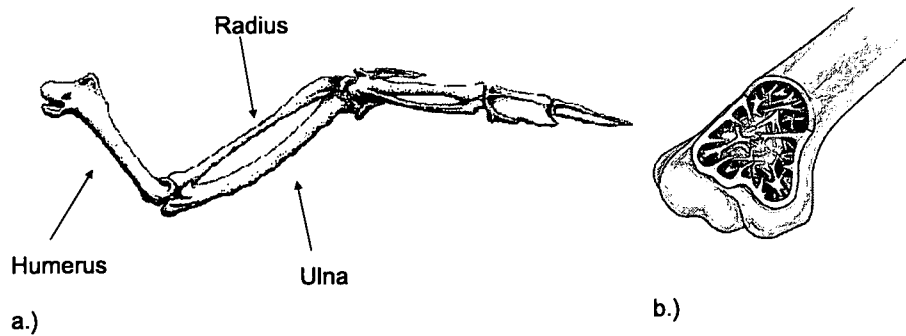


Figure 2.8: Bird Wing Bones

involved in controlling the wing, i.e. changing the camber and planform of the wing during non-steady flight such as takeoff and landing. Without these muscles the birds were still able to perform steady level flight, however they were not able to take off or land independently [24]. Understanding the purpose of the flight muscles is beneficial in understanding the actuator performance that is necessary to replicate the flight motions.

2.2.3 Perching

Birds are capable of morphing their wings to an optimum shape during different flight modes. Some types of flight observed in birds include: cruise, gliding, hovering, and takeoff and landing. For the purpose of this study, the landing, or perching, flight mode was focused on. Mimicking bird motion for MAV morphing development increases the capabilities of the vehicle and improves its functionality. One specific biologically inspired flight capability desired for MAVs is the ability to perch on buildings or other objects to provide remote situational awareness. Including this capability in a MAV's repertoire allows the vehicle to be biomimetic in behavior during landing, further increasing the vehicle's ability to blend in with its environment.

Perching can be defined as landing with approximately zero vertical and horizontal velocity on a specific point. This is achieved by reducing speed while maintaining lift during the landing trajectory. There are several specific maneuvers that birds utilize to complete this type of landing.

During landing, birds often use their strong flight muscles to flap during flight. Because flapping assists in the perching maneuver, it is important to understand the basics of flapping motion. Flapping has been studied in depth by many biologists and aerodynamicists [21, 23, 18, 25, 26, 3]. The flap frequency of several different species of birds was studied by Pennycuik [26]. He fitted an equation to acquired data in order to estimate the flap frequency of a bird based on its mass and wing geometry [26]. Flap frequency is

relevant for many vehicle designs such as the biologically inspired hummingbird wings and experimental testbed apparatus developed by Raney and Slominski [3]. They used their apparatus to simulate vibratory flapping and generate wingbeat patterns similar to those observed in hummingbirds [3]. Most birds adopt some flapping toward the end of their trajectory to generate an additional braking force, similar to a vectored thrust, to slow them down horizontally [17]. Although flapping assists in creating a large drag force and maintaining lift, landing using flapping is energetically expensive and therefore, not ideal for a small vehicle with limited energy supplies.

Alternatively, birds rotate their bodies and wings to very high angles of attack, up to 90 degrees, in order to increase the wing surface area in the direction of the flight path, increasing drag to reduce horizontal flight speed.

In addition, birds often assume an ascending path toward the end of their trajectory [17]. Crowther studied the perching landing maneuver to allow a flight vehicle to land on a point in space [17]. He studied the effect of using a flare maneuver to reach zero vertical and horizontal velocity by altering the landing trajectory. This allowed the vehicle to approach the landing target below and pitch upwards toward the end of the trajectory to gain height and lose speed, ultimately exchanging kinetic for potential energy. This type of trajectory is illustrated in Figure 2.9.

Besides flapping, increasing wing and body incidence, and using an ascending trajectory, birds morph their wing shape by extending the alulae, spreading primary feathers, forming a concave wing section, increasing dihedral, spreading tail feathers, and extending feet among others [21]. Although there are many important shape changes utilized by birds for landing, this project focuses on developing a perching model that utilizes the least amount of degrees of freedom in wings as possible in order to simplify the vehicle design. Therefore, it was decided that the model designed for this project would not flap or change its wing shape to land, but instead utilize different aerodynamic phenomena related to

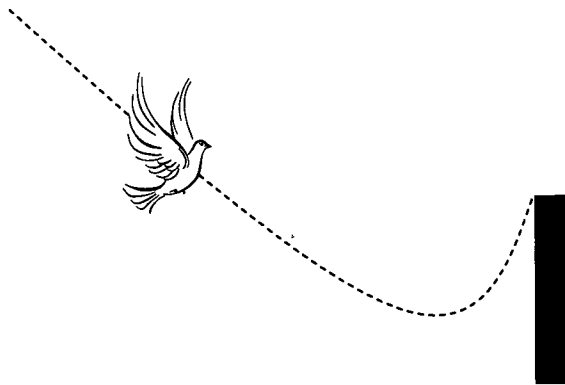


Figure 2.9: Bird-Like Landing Trajectory

high incidence wings and an ascending trajectory, to perch.

2.3 Summary

Many advancements could be made in MAV design that would improve their development. The four major areas in which design could be further researched for improvements includes understanding low Reynolds number aerodynamics, the development of lightweight, flexible and adaptive wing structures, understanding energy storage and conversion to useful power and propulsions and finally, insect like flight navigation guidance and control [8]. This project focuses on developing lightweight and adaptive structures to facilitate perching.

The ultimate goal of this project is to create a MAV that can perch without utilizing flapping. A mechanized model was developed to demonstrate the benefits of wing rotational motion for a perching maneuver as well as to illustrate that size and weight constraints for this type of vehicle can be met utilizing current technology. Wind tunnel testing was completed to analyze the aerodynamic loads on the rotating wings as well as to understand the power requirements of the drive mechanism. Finally, the entire vehicle was modeled analytically for vehicle flight simulation. The analytical results were compared to the wind tunnel results to confirm the accuracy of the analytical model.

The remainder of this thesis will discuss the structural and mechanization design of a bird-like model designed to perch, wind tunnel testing experimental setup and results, and the development of an analytical model for vehicle simulation. The thesis will finish with a discussion of the conclusions made from the project and recommendations for future research.

Chapter 3

Model Design

In order to develop design requirements and determine a limited set of wing degrees of freedom for the perching model, pigeon maneuvers and wing/body kinematics utilized to land were researched. From this understanding, two degrees of freedom were chosen for each wing. These degrees of freedom correspond to wing twist at the shoulder, and a secondary wing twist at the wrist. Once this mechanization concept was determined, pigeon geometry and weight was used for load approximation and structural sizing. Finally, a model was fabricated to incorporate the structure and mechanization. The model consists of a fuselage and attached wings as depicted in Figure 3.1. Notice that the entire span is broken into four sections, symmetrical about the fuselage. The wing actuators, completely contained within the fuselage, allow each section of the wings to rotate up to 90 degrees wing incidence. This chapter will describe the model design in detail.

3.1 Design Concept

One means of landing that birds use is a slow hovering descent in which the bird flaps their wings at a high frequency. Because this method is energetically expensive, very few birds are capable of a hovering descent. Instead, most birds often use a shallow descending trajectory to land. In this method the bird glides or uses powered flight to descend while increasing wing incidence to slow their forward speed. The bird forces the

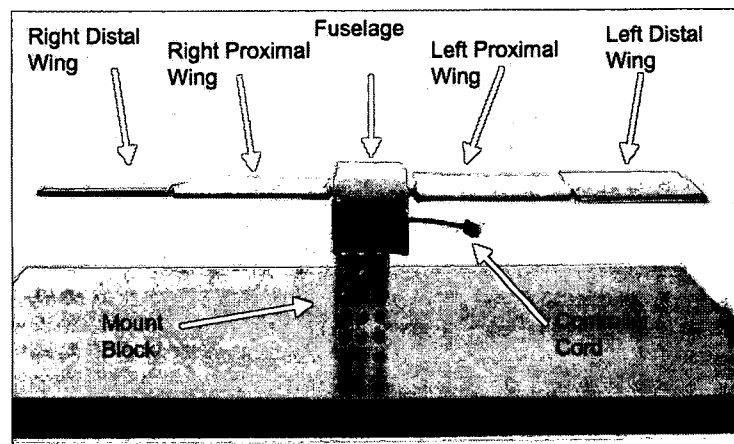


Figure 3.1: Mechanized Model Configuration-Head on View

air flow to stall over the wings, resulting in an energetically cheaper method compared to a hovering landing [27]. Based on this knowledge, the model developed in this study was designed to perch without utilizing flapping, and instead, was designed to be able to rotate its wings up to 90 degrees to reduce horizontal velocity. It was assumed that an ascending path would be necessary to further slow down the vehicle vertically upon approach. Once this concept was selected, the necessary number of degrees of freedom was determined and several design concepts were analyzed.

Comparative scaling techniques developed by Liu as well as geometric scaling relationships developed by Rayner, and measured data collected by Tobalske and Dial were used to determine the approximate geometry of the vehicle [8, 25, 28]. It was decided that the final design would consist of four independent wing panels with actuators confined within the fuselage to mechanize coaxial spars.

3.2 Fuselage

The fuselage was designed to have approximately the same volume as a typical pigeon. The volume of the fuselage was an important design factor because it was previously decided that the wing mechanization and control board would be required to fit within the model. In future iterations of the vehicle, engines, communication devices such as cameras, and a power supply will also need to be contained within the fuselage. Since the focus of this study was to analyze the effects of the rotating wing sections, it was also important that the aerodynamic influence of the fuselage be minimized. Based on these requirements, a symmetrical airfoil with a high thickness to chord ratio, approximately a NACA 0035 oriented at zero degrees angle of attack with flat sides, was selected to be the shape of the fuselage. This airfoil shape was also chosen due to the ease of manufacturability and its reasonable resemblance with the body shape of a bird. The actuators for the

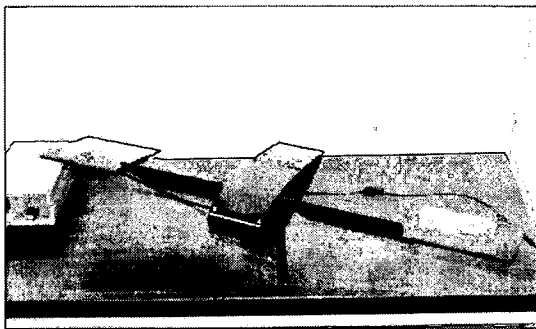
wing mechanization as well as the control board are contained entirely within the fuselage as described later in this chapter.

3.3 Wings

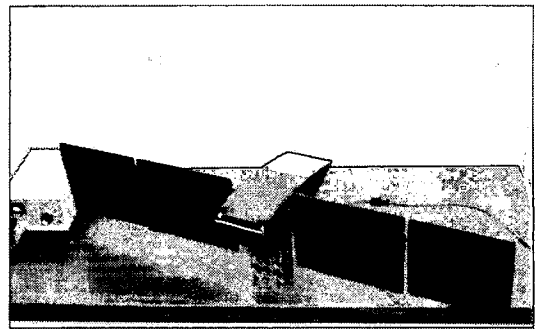
Birds have three joints along each wing: shoulder, elbow, and wrist joints. The goal of this project was to develop a vehicle capable of perching with the fewest degrees of freedom necessary. Therefore, for this design two joints along each wing, one at the shoulder and one at the wrist, were selected. These joint selections resulted in a four wing panel design, with two panels symmetrically on each side of the fuselage. The shoulder joint is located at the root and the wrist joint is located nearly halfway along the span, 14.9 cm from the root. The proximal wing sections (closest to the fuselage) were designed to rotate together, mechanized by a single motor, and a distal wing section (farthest from the fuselage) were designed to be mechanized independently of each other and independently of the proximal panels. To mimic wing motion during perching, the wing panels are capable of rotating to a wing incidence of 90 degrees. The two proximal wings are attached to a single spar driven by one actuator so that they maintain the same wing incidence. These sections of the wing will be flared, or rotated to high angles, throughout the landing trajectory to increase drag thus reducing the horizontal flight velocity. The distal wing sections are each driven by their own independent actuator. These sections of the wings will be used for control during landing. Figure 3.2 shows the model at two different wing configurations.

During landing the wings are not the only part of the bird that rotates. Tobalske and Dial showed that a birds' body angle relative to the horizontal increases with decreasing flight speed [28]. In future iterations of this vehicle, it is possible that not only will the wings rotate, but the body and tail will rotate as well.

Comparative scaling and pigeon geometry was used to determine several of the



a)



b)

Figure 3.2: Model at Two Different Configurations a.)Distal Sections at 10 Degrees and Proximal Sections at 45 Degrees b.)Entire Wing at 90 Degrees

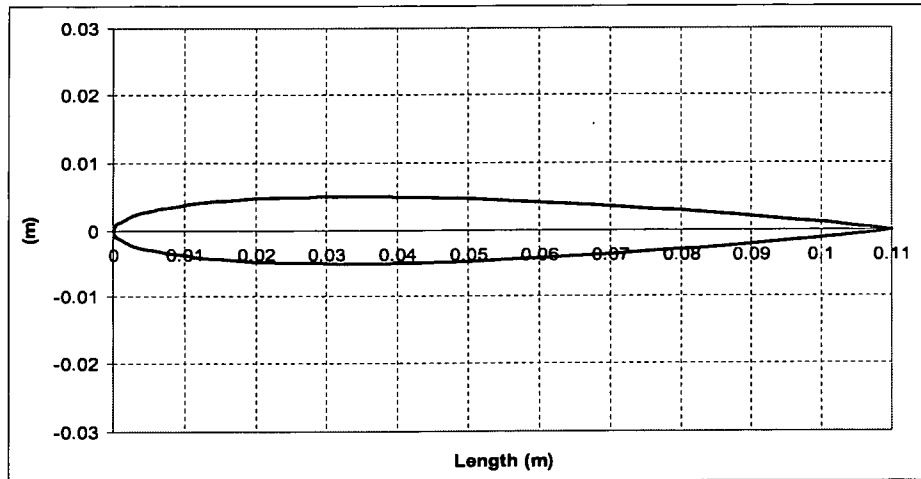


Figure 3.3: NACA 0009 Airfoil Dimensions

geometrical details of the MAV design. The research resulted in a model with a 61 cm wingspan, and a chord of 11 cm [25]. Pigeon wings in general have a drag coefficient ranging from 0.06 to 0.13, a maximum lift coefficient from 0.8 to 1.2, and a maximum lift to drag ratio around 2 to 8 [29]. The thickness ratio, defined as the ratio of maximum thickness to the maximum chord, of the birds studied by Withers ranged from 0.036 to 0.1 [29]. Bird wing thicknesses are very small because feathers account for most of the wings [29]; however, the thickness ratio of the wings in this model was increased to 9 percent, which allows for room within the wings for structural members and actuation. Based on these values, and for the ease of fabrication, a NACA 0009 airfoil shown in Figure 3.3 was selected for the first prototype.

3.3.1 Flight Modes

Since the large wing rotation will only be utilized during landing, an assumption was made to relate wing incidence to flight speed in order to compute maximum design loads. During cruise, at a flight velocity of 10 m/s, both wings will be rotated to 10 degrees. As the

proximal wing sections rotate to a higher angle, drag will increase and the MAV will slow down. It was approximated that a proximal wing section angle of 45 degrees will occur at 7.5 m/s and 85 degrees will occur at 5 m/s. These two flight modes, as well as the cruise flight mode, were analyzed for structural design.

Green and Cheng measured the forces exerted on a perch by pigeons during landing and discovered that the force varied from 2 to 8 times the bird's body weight and that the direction of the force was anywhere from 40 degrees to 90 degrees below the horizontal, with mean flight speeds during this landing ranging from 1.27 to 1.69 m/s [27]. This research implies that a final bird-like vehicle may not land with exactly zero velocity but may need some added force to stop the vehicle. Added drag from the birds body and feet could further slow the vehicle in flight. Pennycuik performed several tests to estimate the drag acting on the body of a wingless bird and found that the average drag coefficient was 0.43. Tests were also completed to estimate the foot drag. Birds used their feet as airbrakes and also fine control. In a fully spread position, it was found that the foot is a highly effective airbrake and has a drag coefficient around 1.10 to 1.25 [30]. The addition of feet in the design could add a significant amount of drag during landing.

3.3.2 Wing Loads

To calculate the forces acting along the wings, several assumptions were made for the first iteration of this design. An elliptical spanwise lift distribution was assumed, and only steady aerodynamics were used. Also, a factor of safety of two was used on all loads for design purposes. High angle of attack data acquired from a study on wind turbines and the previously mentioned assumptions were used to calculate the forces and moments acting spanwise along the wing [7]. The lift and drag coefficients are shown in Figure 3.4 and Figure 3.5 respectively.

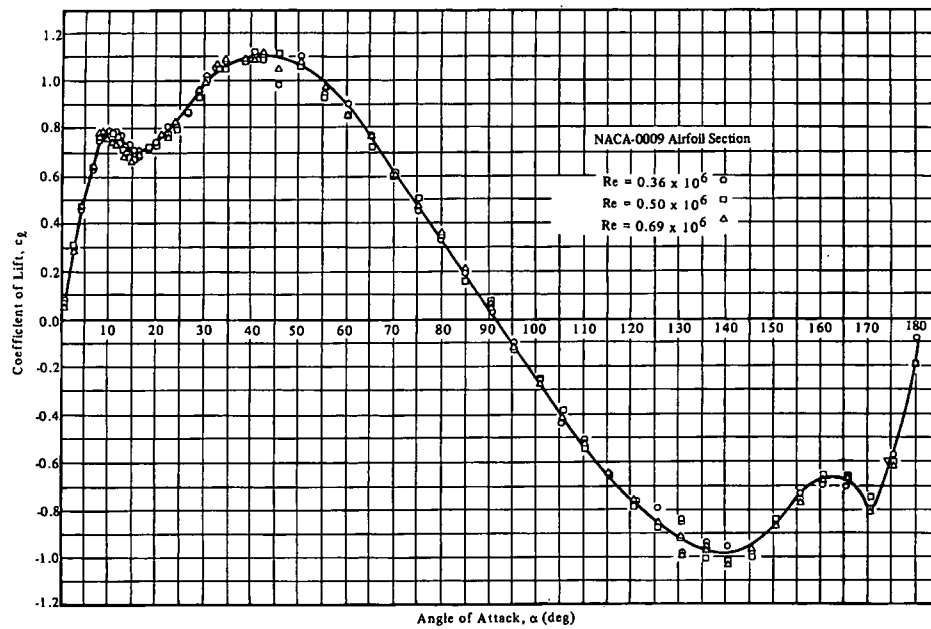


Figure 3.4: Lift Coefficient for Angles of Attack up to 180 Degrees [7]

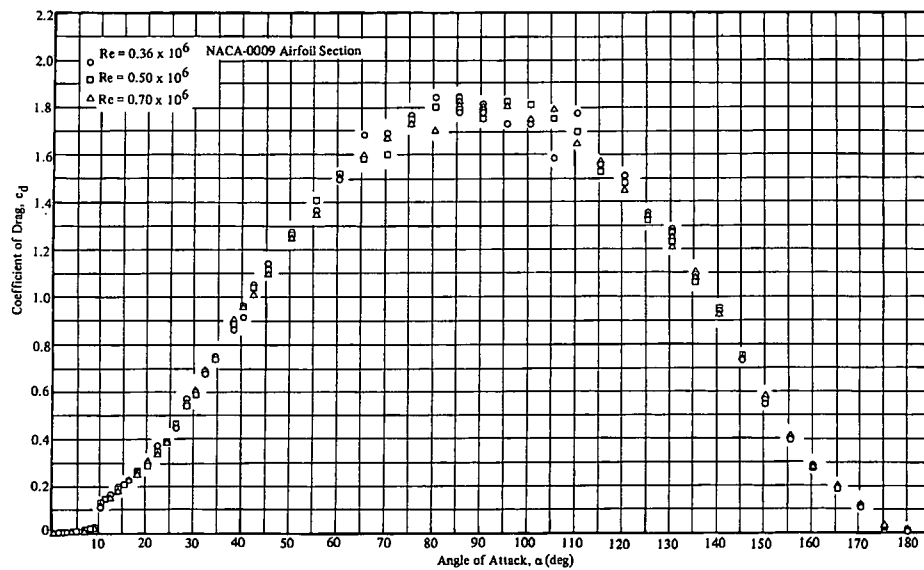


Figure 3.5: Drag Coefficient for Angles of Attack up to 180 Degrees [7]

Table 3.1: Cases Analyzed for Load Calculations

Wing Incidence		Wind Speed (m/s)
Proximal (deg)	Distal (deg)	
10	10	10
45	45	5
85	85	1
45	45	7.5
85	85	5
45	10	5
85	10	1
45	10	7.5
85	10	5

The equation for lift per span, Equation 3.1, was used to determine aerodynamic forces based on 2D aerodynamics (flow over in infinite wing, no flow component in the spanwise direction). More accurate lift data was calculated by using this equation in conjunction with the equation of an ellipse to determine the lift per span acting along a finite wing. Drag per span was also calculated via Equation 3.2 [31].

$$L' = \frac{1}{2} \rho V^2 c_L c \quad (3.1)$$

$$D' = \frac{1}{2} \rho V^2 c_D c \quad (3.2)$$

Where ρ is the density at sea level, V is the velocity, c_L is the lift coefficient, c_D is the drag coefficient, and c is the wing chord. The lift and drag forces were used to calculate shear force and bending moment diagrams for several different cases, shown in Table 3.1. From the calculations, it was determined that the maximum resultant force will occur in the cruise condition, the first case, at 10 m/s with all wing panels at 10 degrees incidence. The lift distribution for this condition, based on an elliptical lift distribution and on 2D lift, is shown in Figure 3.6 and the resulting bending moment is shown in Figure 3.7. These figures show the lift and bending moment from the center of the fuselage out one wing length assuming

that no lift is generated by the fuselage. The elliptical lift calculations resulted in a total lift of 1.57 N for half wing, or a total of 3.14 N. Drag was calculated to be very small, and the maximum bending moment at the center of the fuselage was found to be 0.22 Nm with a bending moment of approximately 0.17 Nm at the wing root. These results influenced the structural design and actuator/spar selection.

3.3.3 Spar

Once the forces and moments acting on the wings were calculated, the main spar, the main load bearing structure in the wings, was designed and the actuators were selected. Since bird bones are generally hollow cylinders, a hollow tube design constructed of carbon fiber tubing was utilized as the main spar. The spar design selected utilizes coaxial cylinders to allow the distal wing sections to be mechanized independently of the proximal wing sections. The proximal spar is a cylindrical tube extending from the elbow joint of the port wing to the elbow joint of the starboard wing. The distal spar is a solid carbon fiber rod that fits inside of the proximal spar allowing it to rotate independently of the proximal spar. This design is shown in Figure 3.8. Two distal spars are used, one for each distal wing section. These spars are connected to actuators inside the fuselage and extend to the tips of the wings. Since the proximal wing panels are dependent of each other, they are connected along a single spar that runs through the middle of the vehicle and attaches to the proximal motor. The distal wings are operated independently. They each have their own spar that fits inside of the proximal spar and ends just short of the center of the fuselage. They each connect to their own distal motor.

The wall thickness of the spar was determined by calculating the maximum shearing stress and maximum bending stress acting on the wing. The polar moment of inertia, Equation 3.3, and the torque or aerodynamic pitching moment, Equation 3.4, were calcu-

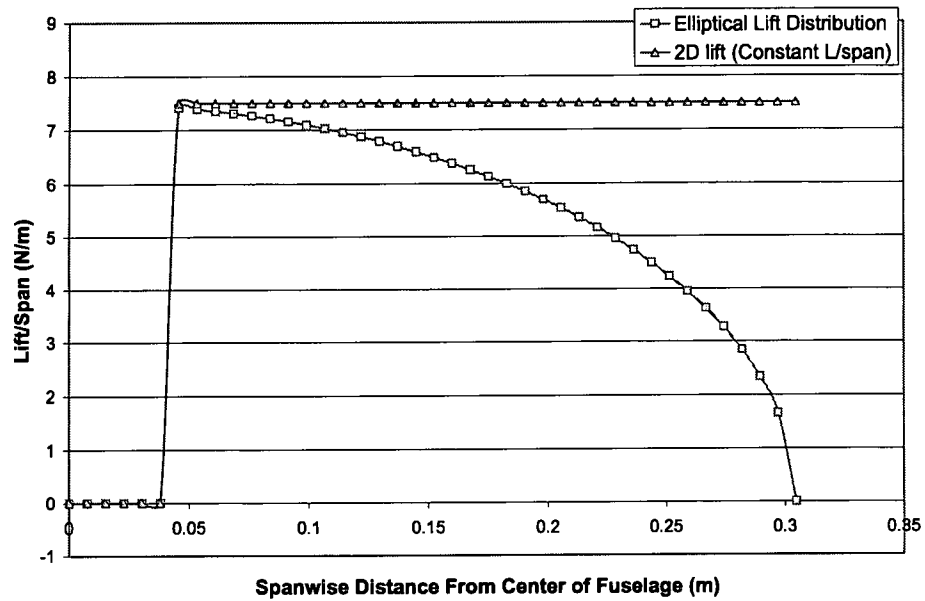


Figure 3.6: Lift Distribution (Wing Panels at 10 Degrees, Speed 10 m/s)

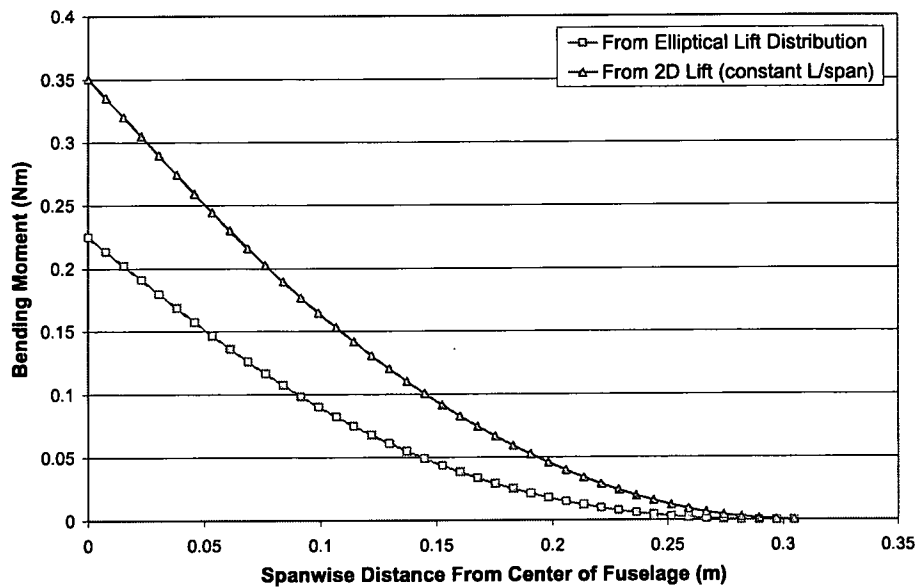


Figure 3.7: Bending Moment (Wing Panels at 10 Degrees, Speed 10 m/s)

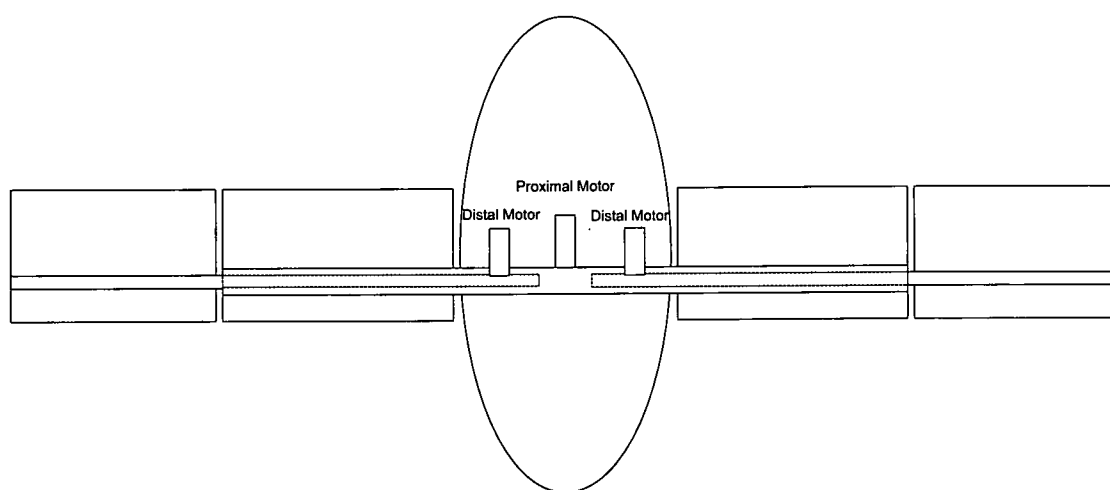


Figure 3.8: Coaxial Cylindrical Spar Design

lated [32].

$$J = \frac{1}{2}\pi(b^4 - a^4) \quad (3.3)$$

$$T = C_M S c \frac{1}{2} \rho V^2 \quad (3.4)$$

Where b and a are the outer and inner diameters respectively of the spar, S is the wing area, and C_M is the aerodynamic moment coefficient. At high wing incidence angles the aerodynamic moment coefficient is much lower, or more negative, than the typical values used. Using an aerodynamic moment coefficient of -0.6 resulted in a torque value of -0.03 Nm for the entire wing. The torque value was imperative for the structural design and for the actuator section because the actuators must be able to work against this torque to drive the wings. The moment coefficient of -0.6 was estimated from geometrical calculations and studies on post stall wind tunnel data for NACA 44XX series airfoils [33].

The maximum shear stress was calculated using Equation 3.5 for several different aerodynamic moment coefficients in order to understand how changing the airfoil shape would affect the shearing stress [34].

$$\tau_{\max} = \frac{Tc}{J} \quad (3.5)$$

Figure 3.9 plots the results for maximum shearing stress for three different moment coefficients. The bending stress was calculated using Equations 3.6 and 3.7. Equation 3.6 is the generic equation for the moment of inertia of a thin walled, hollow circular cylinder [34]. Equation 3.7 was used to calculate the maximum bending stress as a function of maximum bending moment, M_{\max} .

$$I = \frac{\pi(b^4 - a^4)}{4} \quad (3.6)$$

$$\sigma_{\max} = \frac{M_{\max}(\frac{b}{2})}{I} \quad (3.7)$$

Figure 3.10 plots the results for maximum bending stress. Based on this data, it was determined that shearing stress would not be the limiting value for the spar wall thickness

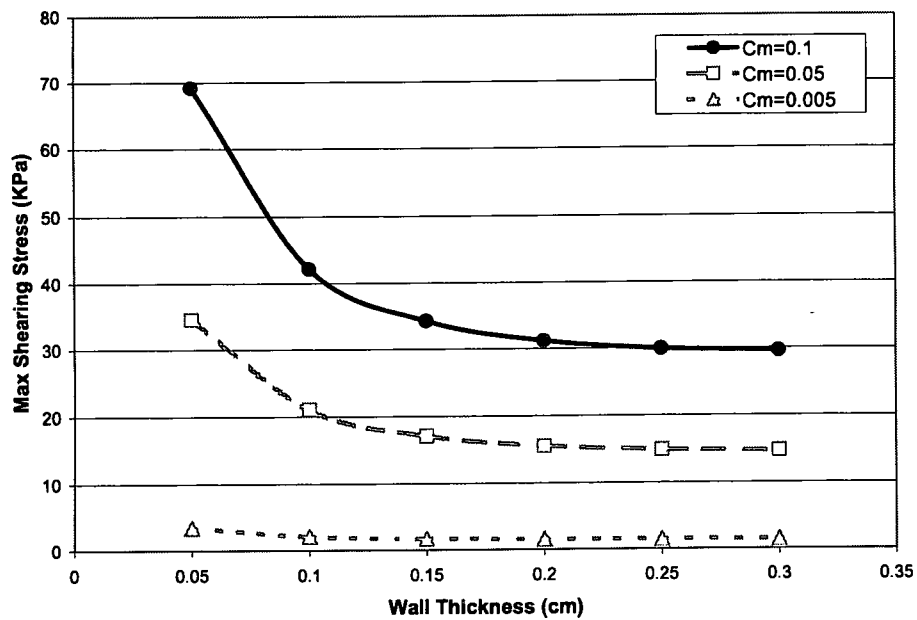


Figure 3.9: Maximum Shearing Stress for Three Generic Moment Coefficients

as the values for shearing stress are much lower than the shear strength of aluminum (2024-T6 Al yield shear strength is 230 MPa). The maximum bending stress was also determined to be much lower than the allowed stress of aluminum (2024-T6 Al allowable bending stress is 350 MPa) [34]. Aluminum was used as a comparison; however, carbon fiber/epoxy tubing was selected for the final design.

The exact material properties of the carbon fiber rods used in the design are unknown. As a comparison, typical carbon fiber epoxy unidirectional composites (IM7/977-3) have an in-plane shear strength of approximately 75 MPa, a longitudinal compressive strength of 1590 MPa, and a transverse compressive strength of 200 MPa [35]. Structural testing utilizing strain gage technology could be used in the future to determine more accurate material properties and structural response for the carbon fiber/epoxy tubing used in this design.

3.3.4 Mechanization

Actuators within the fuselage mechanize the three spars, and therefore the wings, independently. Besides the torque and size requirements previously mentioned, the wing mechanization actuators had to meet several constraints. To estimate a goal actuator weight, bird muscles were researched. The bird flight muscles responsible for wing rotation and thrust generation by flapping typically account for approximately 20 percent of their body mass [23]. Based on this understanding and on a total vehicle mass of 306 g, a goal mass for the actuators and motor was approximately 46 g. Since a motor is not incorporated into this iteration of the design, the actuator mass should actually be much lower than this value. This estimate is a starting point for actuator sizing and selection. Actuator rotation speed was another important aspect to consider when selecting the actuators. Since the distal wings will be used as control surfaces, it was determined that the actuators must be able to rotate the wings quickly, at least 100 degrees per second.

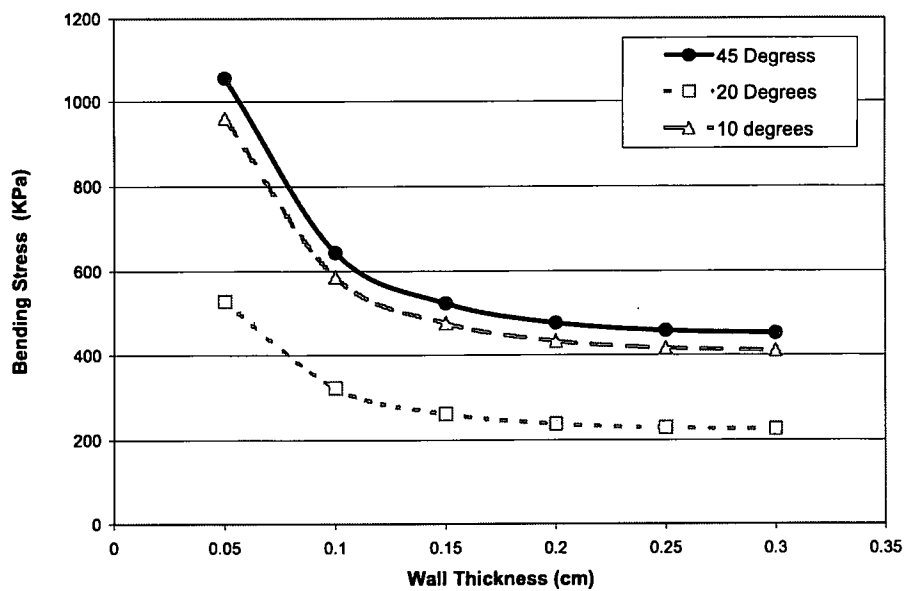


Figure 3.10: Maximum Bending Stress for Three Wing Incidence Angles

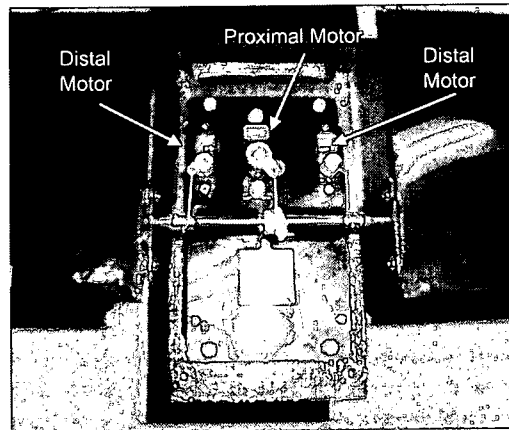


Figure 3.11: Model Actuation

Several different types of actuators were researched to determine the most efficient and practical way to mechanize the wing panels [36, 37, 38]. It was determined that generic servo motors were powerful enough to deliver the required torque for wing actuation. Based on the weight and performance constraints, three actuators were selected for this design. The actuators are basic servo motors with two being identical for mechanization of the distal wing sections and a single, slightly larger, servo motor for mechanization of the proximal wing sections. The distal actuators are Blue Arrow BA-TS-3.6 servos weighing 3.6 g and generating a torque of 0.029 Nm at a no load speed of 0.12 sec/60 degrees. The proximal actuator is a JR S241 Sub-Micro Servo weighing 9 g and generating a torque of approximately 0.069 Nm at a no load speed of 0.18 sec/60 degrees. The total servo motor mass is 16.2 g, at only 35 percent of the estimated actuator and motor mass of 46 g. Figure 3.11 shows the actuation for the wing panels. In the figure, the top cover of the fuselage has been removed to show the internal mechanization of the vehicle.

A control panel, a Parallax Servo Controller-USB(28823) with 16 channels was used to control the motors. The motor control panel and the electrical circuit used for power measurement, described in the next section, were confined within the fuselage. Figure

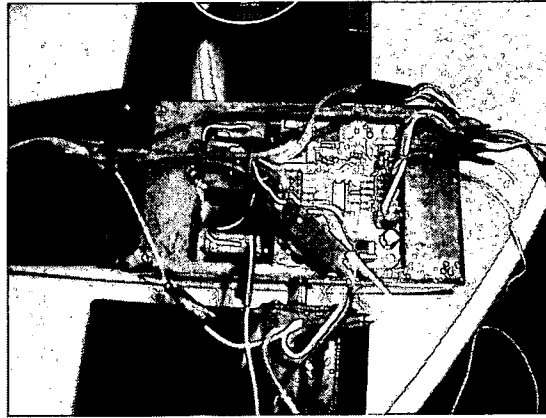


Figure 3.12: Control Panel

3.12 shows the control panel and circuitry for the vehicle with the bottom of the fuselage removed. All of the visible wires are contained completely inside the fuselage when the bottom is replaced. Only the ends of the wires exit through the back of the fuselage so they can be accessed for power measurement

3.4 Fabrication

Detailed design work and prototype construction was completed by Ward Engineering of Columbus, Ohio. The model structure consists of balsa wood with carbon fiber spars and is wrapped in Mylar to insure a light-weight vehicle and a smooth aerodynamic surface. The weight breakdown for several model components are given in Table 3.2. The final model mass is only 158 g which is only 51.6 percent of the maximum mass of 306 g. However, at this time, the vehicle design does not include a tail, landing gear, batteries, a motor, or electronics. In typical fixed wing micro air vehicles the airframe weight fraction is around 40 percent [14]. Therefore, this initial mass appears to be a reasonable value for the wing/fuselage structure and actuation of a complete final design.

Table 3.2: Model Weight Breakdown

Component	Mass (g)	Percent Goal
Goal	306	100
Model	158	51.6
2 Distal Motors	7.2	2.3
Proximal Motor	9	2.9
Control Board	18.7	6.1

Chapter 4

Experimental Testing

To more completely understand and analyze the model, a wind tunnel was utilized for aerodynamic testing. The goal of the wind tunnel tests was to determine if the structure and actuation was robust enough to handle the dynamic forces that would occur during wing rotation. Results obtained from these tests include values for lift and drag at various wing incidence angles and wind speeds. The wing rotation mechanism was powered by an external power source for the wind tunnel tests. Because the vehicle will eventually be powered by an onboard device, the power required to mechanize the wings under loaded conditions was also measured.

This wind tunnel test also was completed to better understand the dynamic and post stall effects on the wings and the power required to drive the actuation motors. Future tests will be completed to obtain more accurate measurements. This first test provided a way to understand the order of magnitude of the forces that could be expected during a typical landing trajectory and to discover faults in the experimental procedure.

4.1 Wind Tunnel Test

4.1.1 Tunnel Description

Wind tunnel tests were completed in the University of Dayton's low speed wind tunnel. The tunnel is a closed test section, open air tunnel with a square cross-sectional area

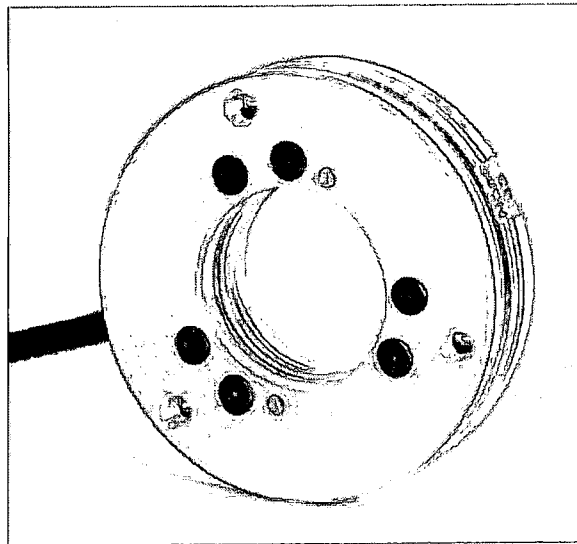


Figure 4.1: Nano43 Force Transducer

of 76.2 by 76.2 cm. The tunnel flow speed can be adjusted by controlling the fan motor speed. A honeycomb grid at the front of the tunnel splits and damps vortices to reduce turbulence intensity. Speeds from 1-10 m/s were used during the testing. At speeds lower than 5 m/s, there was a significant amount of turbulence in the flow due to the atmospheric conditions and wind gusts outside the tunnel. It was difficult to precisely measure the wind speed during testing using the pitot tube device that was available, especially at speeds under 5 m/s. There was also some error in other atmospheric condition measurements that led to uncertainty in the results.

4.1.2 Force Transducer

A Nano43 six axis force transducer from ATI Industrial Automation was used to measure the aerodynamic forces acting on the model. The Nano43 is shown in Figure 4.1. Physical specifications for the Nano43 are given in Table 4.1. This data includes the single axis overload values and the geometrical specifications. A specific calibration was selected for the sensor. The details of the selected calibration, including the sensing ranges

Table 4.1: Specifications for Nano43

Single Axis Overload	
Fxy	± 300 N
Fz	± 400 N
Txy	± 3.4 N-m
Tz	± 45.3 N-m
Physical Specifications	
Weight	0.039 kg
Diameter	43 mm
Height	12 mm

and resolution, are given in Table 4.2. Because the data acquisition system in the wind tunnel was set to measure and record data in the English system of units, the calibration selected for this sensor was in English units. The supplier, ATI Industrial Automation, does provide an equivalent calibration in metric units shown in Table 4.3

4.1.2.1 Calibration

Before any wind tunnel testing could be completed, the Nano43 force transducer had to be calibrated. The results from the calibration were used to translate between the 6 degree of freedom forces measured at the load cell and the 6 degree of freedom forces at the vehicle center of gravity. It was later discovered that the calibration stand was not exactly square on all edges. The unevenness of the stand and human error in the calibration routine resulted in a final calibration matrix that was significantly inaccurate. Since the goal of the experiment was to determine the structural response of the model and order of magnitude for the loads, the error in the calibration was not considered to be a critical problem. However, these inaccuracies did add significantly to the uncertainty in the final load results. Figure 4.2 shows one position used to calibrate the load cell and the stand apparatus that was used for the calibration. Several different configurations of

Table 4.2: Actual Calibration for Nano43

Calibration	Fx,Fy	Fz	Tx,Ty	Tz	Fx,Fy	Fz	Tx,Ty	Tz
US-8-4	8 lbf	8 lbf	4 lbf-in	4 lbf-in	1/2320lbf	1/2320lbf	1/4640lbf-in	1/4640lbf-in
	Sensing Range				Resolution			

Table 4.3: Metric Calibration for Nano43

Calibration	Fx,Fy	Fz	Tx,Ty	Tz	Fx,Fy	Fz	Tx,Ty	Tz
SI-36-0.5	36 N	36 N	500 N-mm	500 N-mm	1/128 N	1/128 N	1/10 N-mm	1/10 N-mm
	Sensing Ranges				Resolution			

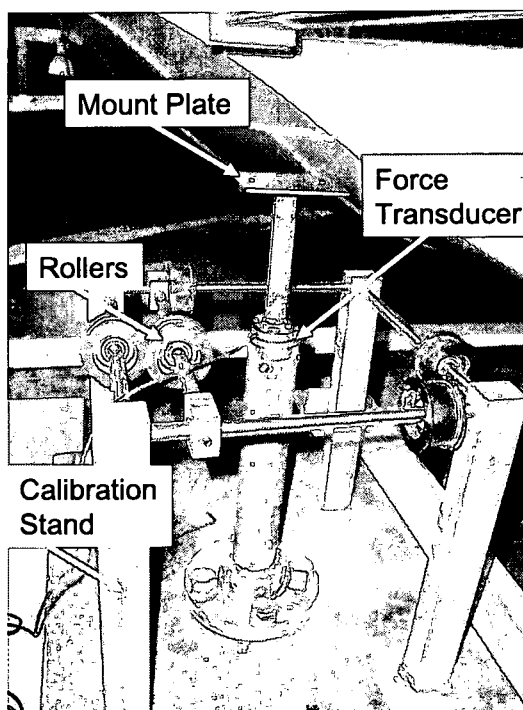


Figure 4.2: Calibration Setup

the sting, calibration stand, and a t-arm were used for the calibration. Weights were hung on the ends of a t-arm connected to the mount plate in increments of 50 grams, from 0 to 300 grams for the calibration. The rollers were used to insure that the loads were applied in the correct planes and were aligned correctly. The calibration curves are given in the appendix. The results were used to develop a calibration matrix using Equation 4.1.

$$[SG] = [CM][F] \quad (4.1)$$

Where $[SG]$ measures the voltage vector from the six strain gages in the load cell, $[CM]$ is a 6x6 coefficient matrix containing the calibration curve slopes, and $[F]$ is a 6x1 applied load vector.

4.1.3 Test Setup

Figure 4.3 illustrates the experimental setup for the wind tunnel testing. For the wind tunnel test three computers were used. One computer was programmed to control the actuators that moved the wings to specific angles. Although the angles were programmed into the computer and accurately measured, free play in the model slightly altered the wing incidence angles during the test. The actual angles were sometimes as much as 10 degrees different from the programmed angles. The protractor mounted on the side of the tunnel allowed for actual angle measurement during the test. To control the wings, the model had to also be connected to a power supply set to deliver a constant 4.5 V. A second computer was used for data acquisition. This computer used a LabView code programmed to measure the aerodynamic forces and moments utilizing the calibration matrix discussed above. This computer was connected to a data acquisition system connected to the Nano43 force transducer. The system measured and recorded lift, drag, side force, pitching moment, rolling moment, and yawing moment at a sampling rate of 1000 Hz. Finally, a third computer was used to record voltage data to be for power measurement. This

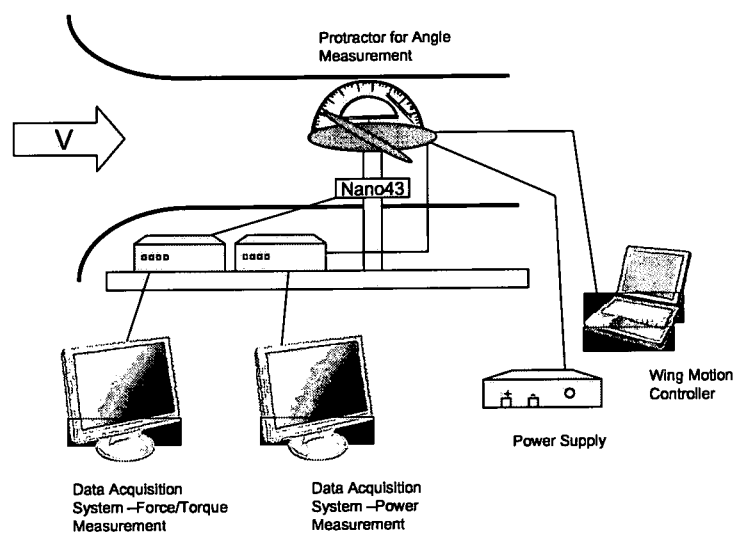


Figure 4.3: Wind Tunnel Experimental Setup

computer was connected to a data acquisition system that utilized 4 channels to measure 4 voltages. The measured voltages included the voltage into the proximal motor, voltage into the distal motor, voltage across the proximal resistor, and voltage across the distal resistor. This data was later used to calculate power.

The model was mounted on a single strut from the bottom of the tunnel designed specifically to connect with the model and the force transducer. The strut positioned the model in the center of the test section vertically and horizontally. During testing, the force transducer was located 12.86 cm directly below the aerodynamic center of the vehicle. A camera was positioned in line with the model to photograph the wings at different angles. Wires for the motor control and voltage measurement came out of the back of the fuselage and ran along the backside of the sting through a hole in the bottom of the tunnel. Figure 4.4 shows this setup.

In order to visually determine the wing panel angles, colored needles were attached to the leading edge of the wings as shown in Figure 4.5. Photographs were later used to determine the angle of the wing panels. The different colored needles made it easier to distinguish between the two sections.

4.1.4 Test Procedure

Several tests were completed in the wind tunnel with varied wind speed and wing section angle changes. The wind speed varied from 1 m/s to 10 m/s between tests. The wings rotated from 0 to 10, 45, or 85 degrees depending on the wind speed, and also rotated from 10, 45 or 85 degrees back to 0 degrees. The model was positioned in the center of the tunnel at the beginning of the test procedure. For each test the atmospheric conditions were recorded and the wind speed was set by adjusting the tunnel fan speed and measuring the actual speed using the pitot tube device. Once the wind speed was steady, one computer was used to control the wing movement and two separate computers

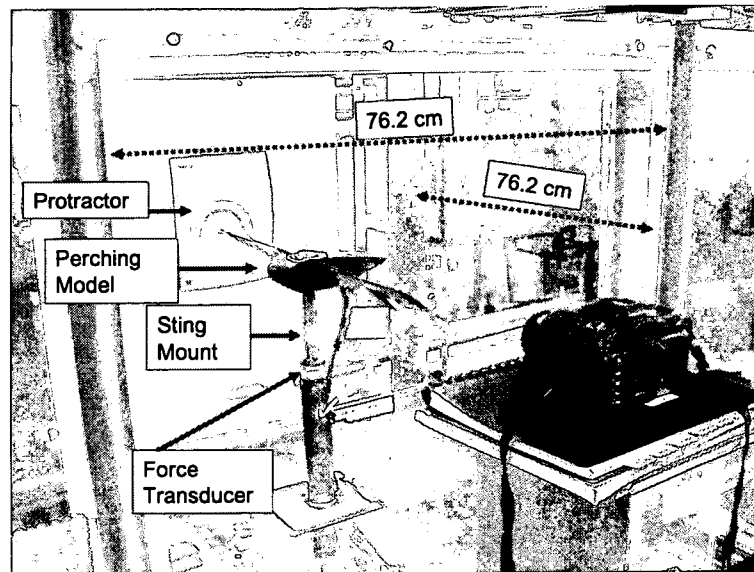


Figure 4.4: Model Position in Wind Tunnel

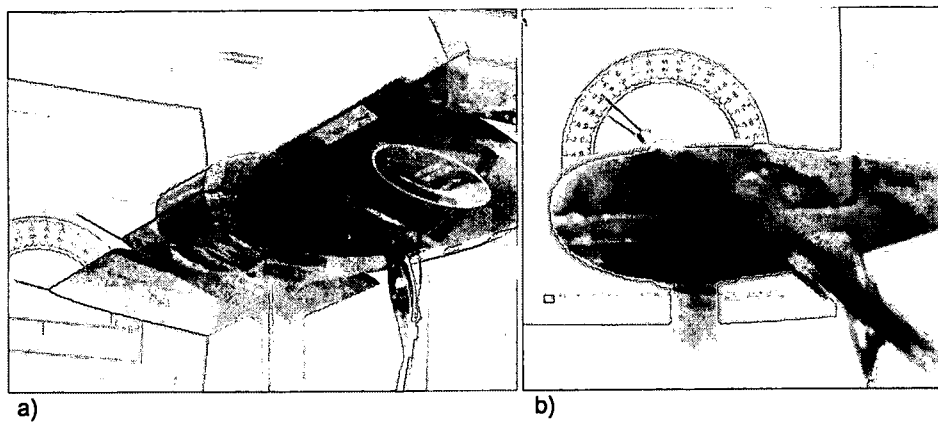


Figure 4.5: Wing Incidence Measurement

were used to record the data. At the beginning and end of each test the wind speed, atmospheric conditions, and the wing incidence for each panel were recorded. The test matrix used for the wind tunnel tests is shown in Table 4.4. The angles specified in the tests matrix are the programmed angles not the actual angles achieved during testing.

4.1.5 Results

The goal of the wind tunnel tests was to determine if the structure and actuation was robust enough to handle the dynamic forces that would occur during wing rotation. This wind tunnel test was also completed to better understand the power required to drive the actuation motors. Future tests will be completed to obtain more accurate measurements. This first test also provided a way to understand the order of magnitude of the forces that could be expected during a typical landing trajectory and to discover faults in the experimental procedure.

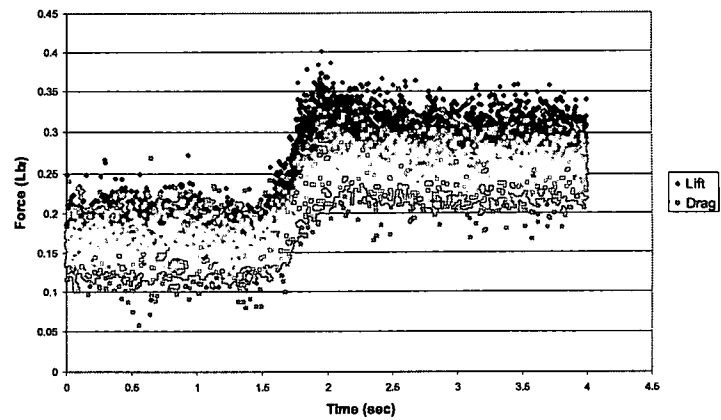
Results from the wind tunnel tests include measurements of lift, drag, side force, pitching moment, rolling moment, and yawing moment as well as power for each motor. Due to inaccuracies in measurement techniques and an inaccurate power circuit, only the lift and drag data is focused on in this section. Benchtop tests were completed to more accurately measure power requirements as discussed in the next section. After testing was performed, an aerodynamic tare approximation and data filtering was completed to more accurately analyze the results. Blockage and wall interference corrections also were considered after the data was filtered. Once corrections were accounted for and filtering was completed, the results from the wind tunnel testing were analyzed to determine trends.

4.1.5.1 Data Filtering

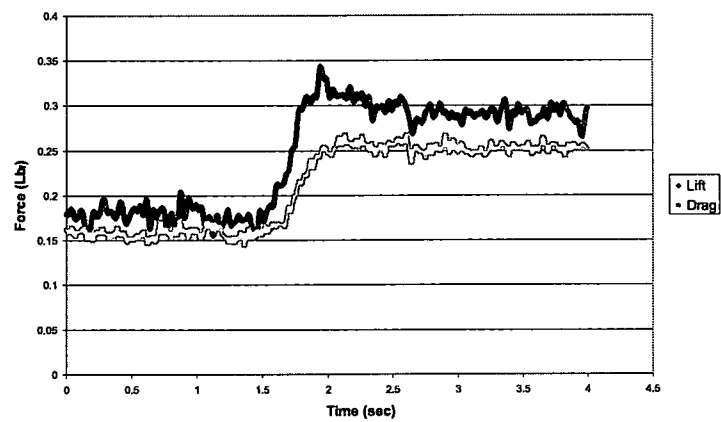
A 8th order lowpass digital Butterworth filter with a normalized cutoff frequency of 25 Hz ($W_n=0.05$) was used to filter the wind tunnel data. Figure 4.6 compares the lift and

Table 4.4: Wind Tunnel Test Matrix

Test Number	Velocity (m/s)	Proximal Angle (Deg)		Distal Angle (Deg)	
		Start	Finish	Start	Finish
1	1	Aerodynamic Tare			
2	5	Aerodynamic Tare			
3	7.5	Aerodynamic Tare			
4	10	Aerodynamic Tare			
5	1	0	0	0	0
6	1	0	85	0	10
7	1	85	85	10	10
8	1	85	85	10	85
9	1	85	85	85	85
27	1	85	0	85	0
10	5	0	0	0	0
11	5	0	45	0	10
12	5	45	45	10	10
13	5	45	45	10	45
14	5	45	45	45	45
28	5	45	0	45	0
15	5	0	85	0	10
16	5	85	85	10	10
17	5	85	85	10	85
18	5	85	85	85	85
29	5	85	0	85	0
19	7.5	0	45	0	10
20	7.5	45	45	10	10
21	7.5	45	45	10	45
22	7.5	45	45	45	45
23	7.5	45	0	45	0
30	7.5	0	10	0	10
31	7.5	10	10	10	10
33	7.5	5	5	5	5
24	10	0	0	0	0
25	10	0	10	0	10
26	10	10	10	10	10
32	10	10	0	10	0
34	1	All Motions with Tunnel Off			



a)



b)

Figure 4.6: Comparison of Raw Verses Filtered Data: a)Raw Data for Test 22 b)Filtered Data for Test 22

drag data for test 22 before it was filtered and after the filter was used. As shown, the resultant data is much clearer and easier to interpret. This filter was applied to all of the wind tunnel data.

4.1.5.2 Interference Corrections

Solid blockage and wall interference corrections were estimated based on the methods described in *Low Speed Wind Tunnel Testing* [39].

After the testing was completed and the data was filtered, some corrections had to be made to the data. One issue was the solid blockage of the test section due to the model. The blockage is defined as the frontal area of the model divided by the test section area. In the worst case, with all the wing panels at 90 degrees, the solid blockage was found to be approximately 10.6 percent. Various sources have different opinions on when solid blockage should be corrected for. Some sources recommended correcting for anything over 7.5 percent, others 10 percent or even 5 percent [39]. Regardless of which source is correct, in this situation the blockage should be corrected for. However, to calculate blockage corrections, the wind tunnel boundary layer needs to be known. In this case, this value is unknown and calculations were not completed. Since there were many uncertainties in the testing, the small correction due to blockage is not critical.

Another correction that needed to be made for this test was due to wall interference. Wall interference is generally corrected for when the span of the model exceeds 80 percent of the tunnel width. One restriction on the model design was directly related to this value. It was known that the 76.2 cm wide test section would be used for tunnel testing, therefore, the wingspan of the model was restricted to 80 percent of the width, or in this case, 61 cm. This is exactly what the final wingspan of the model was designed to be. Therefore, the model span was at the maximum recommended for tunnel testing and therefore wall interference corrections were made. Using the equations for a closed rectangular tunnel,

taper ratio of 0 and an aspect ratio of 6, results in a boundary correction factor of 0.16 for uniform loading and 0.15 for elliptical loading. The corrections for wall interference can be calculated using Equation 4.2.

$$\Delta\alpha = \delta \left(\frac{S}{c} \right) C_{LW}(57.3) \quad (4.2)$$

The corrections for lift coefficient for each wing angle are given in Table 4.5. The table shows that although the wings are at a specific geometric angle, the correction factor increases the angle and thus alters the lift coefficient. Again, since there are several uncertainties in the test results, these correction factors do not play a large roll in the analysis.

4.1.5.3 Aerodynamic Forces and Moments

As previously mentioned, at speeds below 5 m/s the wind tunnel data is innaccurate. Figure 4.7 demonstrates this issue. This figure shows the lift and drag plots for two different tests, test 6 and test 15. In both of these tests all the wing panels started at 0 degrees wing incidence and the proximal panels moved to 10 degrees while the distal panels moved to 85 degrees. The difference between the two tests is only the wind speed. In test 6, the wind speed was set to approximately 1 m/s and in test 15, the wind speed was set to approximately 5 m/s. Since both tests were operated at two different speeds, the values of the forces are expected to be different, however, the trends should remain the same. The plot for test 6 illustrates the type of results that were obtained for tests at around 1 m/s. At this speed the data does not capture the changes in force as the wing angles change. The change in force is possibly too small for the data acquisition system to pick up and noise from the system blocks the results. Because of this issue, only tests at and above 5 m/s were analyzed. The wind tunnel results often shown negative values for the lift and drag forces. This is due to inaccurate calibration which would cause the curves to shift. The negatives lift values could also be due to inaccurate angle measurements; although

Table 4.5: Wall Interference Corrections

Geometric Angle	Corrected Angle	Geometric C_L	Corrected C_L
-5.00	-6.66	-0.50	-0.30
-3.00	-4.00	-0.30	-0.43
-2.00	-2.67	-0.20	-0.30
0.00	0.00	0.00	0.00
2.00	2.67	0.20	0.30
3.00	4.00	0.30	0.43
4.00	5.43	0.43	0.55
5.00	6.50	0.45	0.60
6.00	7.83	0.55	0.70
8.00	10.33	0.70	0.80
10.00	12.66	0.80	0.75
12.00	14.49	0.75	0.72
13.00	15.39	0.72	0.72
19.00	21.43	0.73	0.75
20.00	22.49	0.75	0.75
27.00	29.86	0.86	0.95
30.00	33.16	0.95	1.05
33.00	36.49	1.05	1.09
35.00	38.59	1.08	1.10
36.00	39.62	1.09	1.10
37.00	40.59	1.08	1.10
38.00	41.66	1.10	1.12
40.00	43.66	1.10	1.12
43.00	46.72	1.12	1.08
44.00	47.66	1.10	1.08
45.00	48.59	1.08	1.08
70.00	72.00	0.60	0.60
78.00	79.23	0.37	0.35
80.00	81.16	0.35	0.30
82.00	83.00	0.30	0.30

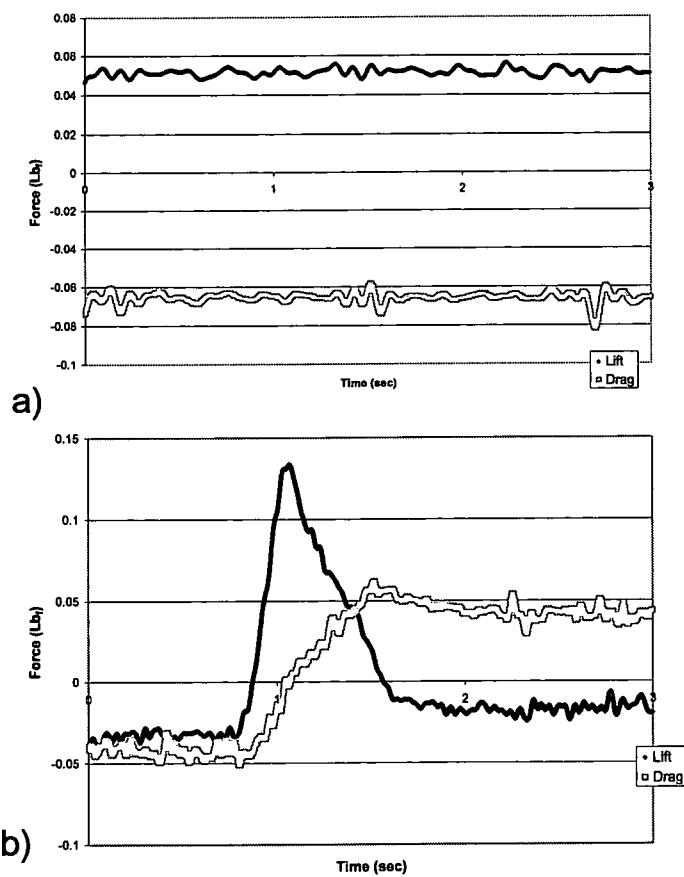


Figure 4.7: Comparison of a) 1 m/s to b) 5 m/s Test

Table 4.6: Wind Tunnel Test Details

Test Number	Tunnel Velocity (m/s)	Angle Commanded (Deg)				Angle Achieved (Deg)			
		Proximal Start	Proximal Finish	Distal Start	Distal Finish	Proximal Start	Proximal Finish	Distal Start	Distal Finish
15	5	0	85	0	10	2	82	2	6
20	7.5	0	45	0	10	0	35	0	4
22	7.5	45	45	40	45	40	40	4	30
29	5	85	0	85	0	80	0	70	0

the wing angles were thought to be at zero degrees, they could have actually been slightly negative which would cause this results. The negative drag values could be due to an inaccurate tare approximation.

Four different tests are described in this section; other test results are presented in the appendix. These tests: test 15, 20, 22, and 29 were chosen to represent a variety of wing motions and the associated lift and drag trends. During several of the tests, the commanded wing incidence angle and the actual angle achieved were slightly different as a result of free play in the model linkages. The details for the tests are presented in Table 4.6.

Figures 4.8, 4.9, 4.10, and 4.11 show the lift and drag results for four different tests. For each test, two plots are given. The top graph shows the lift and drag forces as a function of time, and the bottom graph shows the corresponding wing incidence angle for the proximal and distal panels. By analyzing these four tests, an understanding of the effects of the wing motion and the forces associated with the different motions can be developed.

According to lift coefficient data for the NACA 0009 airfoil, the wings should stall at a wing incidence of approximately 10 degrees [4]. Trends also show that after stall the lift coefficient should initially decrease, but begin to increase again at 15 degrees due to the

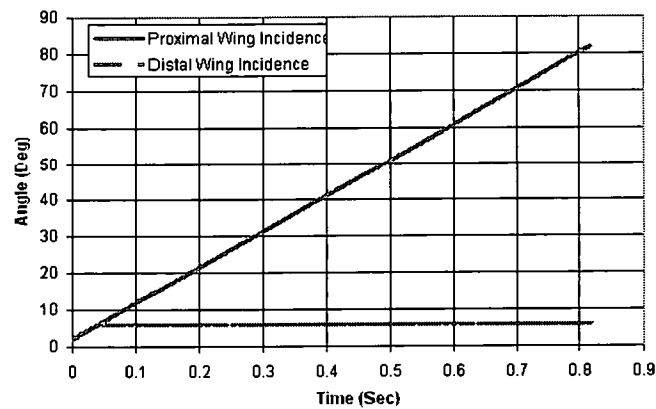
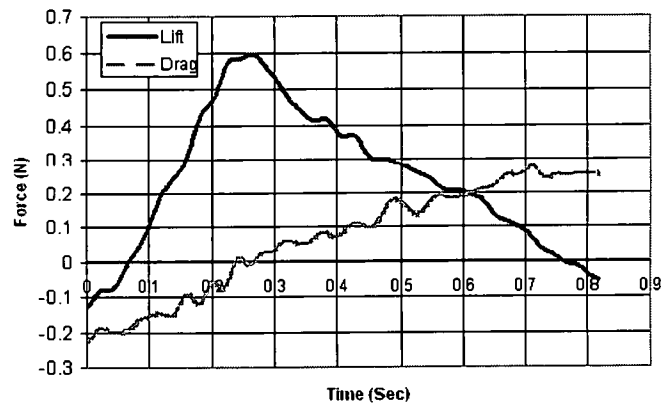


Figure 4.8: Lift and Drag for Test 15, 5 m/s

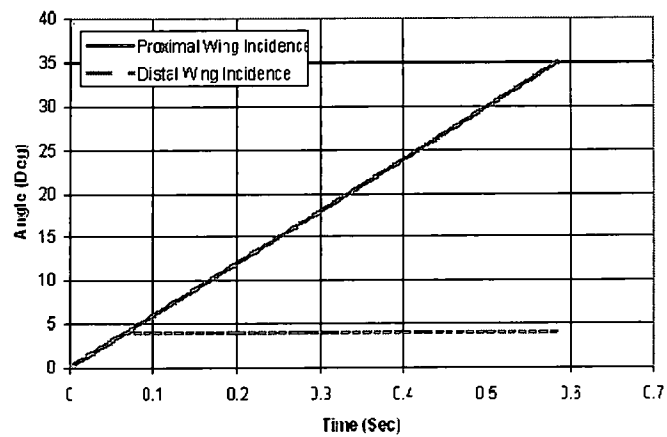
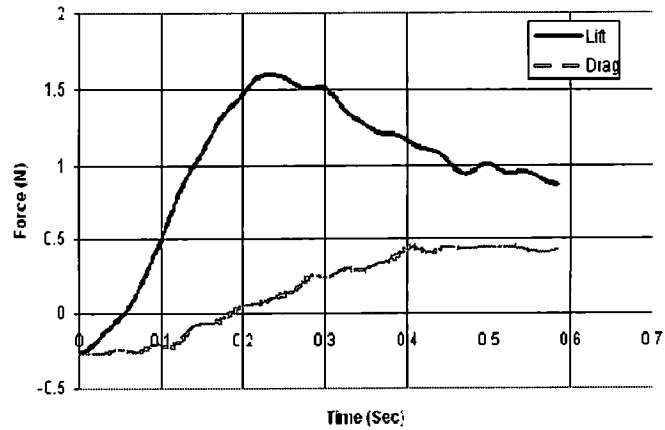


Figure 4.9: Lift and Drag for Test 20, 7.5 m/s

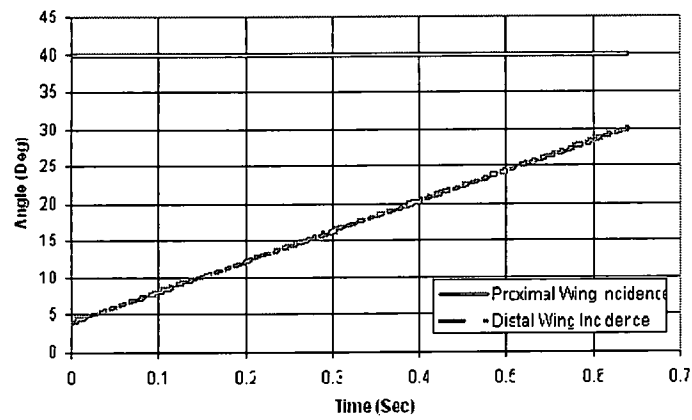
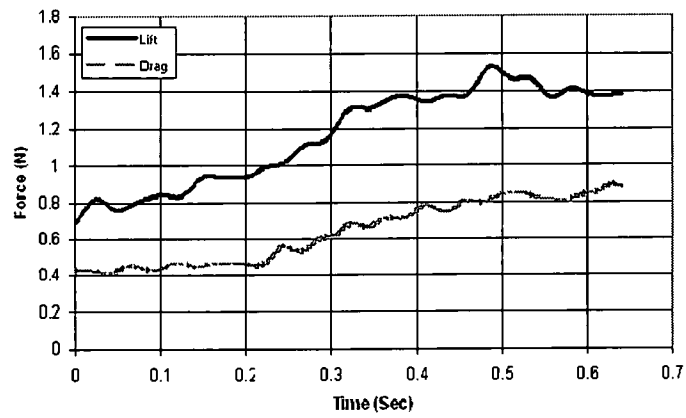


Figure 4.10: Lift and Drag for Test 22, 7.5 m/s

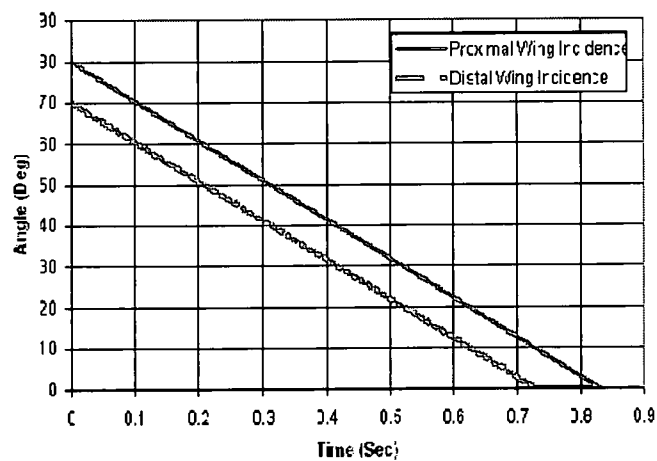
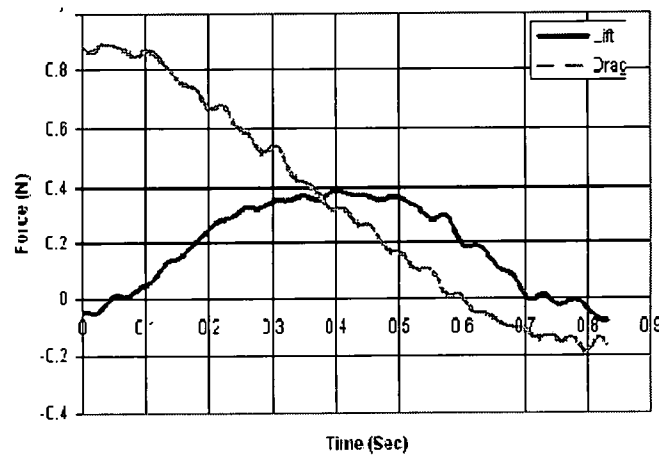


Figure 4.11: Lift and Drag for Test 29, 5 m/s

pure resultant forces acting on the wing. The maximum lift is reached as a wing incidence angle reaches 45 degrees. At this point, the lift coefficient again decreases. The lift curve for several of the tests does not exactly mimic this data; instead, dynamic effects due to the wing rotation cause unexpected results.

In test 15 the wind speed was set to approximately 5 m/s. While all four wing panels were programmed to start at approximately zero degrees wing incidence, photographs later showed that the wings actually started at around 2 degrees. This error is due to free play in the model linkages. The proximal panels moved linearly with time to approximately 82 degrees incidence, and the distal panels moved simultaneously to 6 degrees incidence. All sections moved at the same speed resulting in the proximal and distal wings at the same angle up to 6 degrees. At this point, the distal wings finished rotating while the proximal panels continued to rotate up to 82 degrees. The results from test 15, shown in Figure 4.8, do not show an initial stall at 10 degrees as expected. The lift curve shows that a lift decline finally occurs when the distal wings are at 6 degrees and the proximal wings have reached approximately 28 degrees. The secondary lift peak, expected from a quasi-static response, is not evident. During this test, the wing incidence pitch rate was relatively high, 80 degrees in 0.8 seconds, resulting in the observed stall point at about 28 degrees wing incidence. The higher than expected stall angle could be a demonstration of dynamic stall. The drag curve shows that the drag increases almost linearly as the wing incidence increases. The maximum lift value for this test is fairly lower than was expected. This error could be due to inaccurate calibration, wind speed measurements, or wing incidence measurement techniques.

In test 20 the wind tunnel speed was set to approximately 7.5 m/s and the proximal wing panels were programmed to begin at 0 degrees and rotate linearly to 45 degrees. The distal wing sections were also programmed to start at 0 degrees but rotated with the proximal sections up to 10 degrees where they stopped rotating and remained at 10

degrees while the proximal wing panels finished their rotation to 45 degrees. Photographs later showed that the distal wings actually only rotated to 4 degrees and the proximal wing sections rotated only to 35 degrees. As the wing sections began to rotate, the lift force increased as shown in Figure 4.9. At around 14 degrees the wing surface stalled and the lift began to decrease. For test 20, the pitch rate is relatively slow, 35 degrees in 0.6 seconds, and the expected quasi-static response is observed with a stall point at approximately 14 degrees. The lift was expected to increase after stall; however, it is not unreasonable due to the uncertainties in the testing that we do not see a second peak. The drag increased during the rotation as expected.

During test 22 the wind tunnel speed was set to approximately 7.5 m/s and the proximal wing sections were programmed to remain at 45 degrees throughout the entire test. The distal wing sections were programmed to start at 10 degrees wing incidence and rotate to 45 degrees. Photographs taken during the test showed that the proximal wing sections were actually positioned at approximately 40 degrees during the entire test and the distal wing sections started at 4 degrees and rotated to 30 degrees. Figure 4.10 shows the results for lift and drag during the rotational portion of the test. As the distal wings rotated, the lift initially increased until around 24 degrees when it started to decrease. During this test, lift was dominated by the proximal wing sections which are already post stall, resulting in a reduced effect of the outer wing stalling in such that the distal wing stall is not readily discernable. The drag also increased throughout the test as the distal wing angle increased.

In test 29 the wind tunnel speed is set to approximately 5 m/s and all wing sections were programmed to rotate from 85 degrees to 0 degrees. However, photographs taken during the test showed that the proximal wings actually started at 80 degrees and ended at 0 degrees and the distal wing sections started at 70 degrees and rotated to 0 degrees. Figure 4.11 shows the lift and drag data for the rotational part of this test. The lift data

shows that the lift increases as the angle of the wings rotate until the panels reach approximately 30 degrees for the distal panels and 40 degrees for proximal panels. At this point, the lift peaked and started to decrease. The results show the classic shape of the lift curve; however, stall is not readily discernable due to hysteresis. Prominent stall on reattachment when reducing wing incidence is rarely evident. The drag also decreases throughout the test as was expected.

In all of the tests, either the starting or ending values for lift and drag were found to be slightly negative. It is possible that the incidence of the wings was actually slightly negative which would result in a negative lift at the beginning of the motion. The slightly negative drag at the beginning of the motion could be due to error in calibration or in the aerodynamic tare approximation. The aerodynamic tare was completed with the sting mount in the tunnel without the model at different speeds to determine the drag effects from the sting. Again, the error in the force values could be due to the wall or solid blockage interference, the inaccurate calibration matrix, or inaccuracy in the angle and flow speed measurements.

From the results of the wind tunnel tests, it appears that some dynamic effects take place during the wing rotation that lead to varied stall angles. Due to the high pitch speed of the wind panels, it is possible that dynamic stall is occurring during some of the tests. Utilizing dynamic effects such as dynamic stall by optimizing wing rotation could improve the perching ability of the vehicle by providing an extra lift effect toward the end of the landing trajectory. Further investigation of this phenomenon must be studied in order to understand the flow physics of the post stall rotating wings. One study, completed at NASA Langley Research Center studied the effect of wing pitch rate on dynamic stall effects and found that at a constant pitch rate the lift coefficient was increased by up to 0.6 [40]. This study provides an estimate of the benefits that dynamic stall can have on the perching vehicle.

4.1.5.4 Other Results

There were other important results obtained during the wind tunnel tests besides the trends and order of magnitude lift and drag forces at different wind speeds and wing angles. The wind tunnel tests proved that the vehicle is structurally sound enough to withstand the forces expected during a typical perching trajectory including those associated with dynamic effects. During some of the tests, slight vibrations were visually observed in the distal wings. These vibrations were due to the free play in the actuation linkages. The model could be improved if the free play was reduced. The wind tunnel test was a success in that it verified that the model was structurally sound, and that the actuation had the required torque to actuate the wings under the loaded condition. There were some inaccuracies in the measurements; however, these issues can be resolved for future tests.

4.1.5.5 Uncertainties

As previously mentioned throughout this section, there were several experimental uncertainties that caused the wind tunnel results to be inaccurate. Errors in the calibration matrix added greatly to this uncertainty. This error could result in as much as a 0.5 N difference between the actual lift and drag measurements and the results. The results that were found during the testing could be as much as 0.5 N lower than the actual forces acting on the model. Another error is due to the angle measurement techniques. Free play in the model linkages caused a wing panel angle change under the loaded condition that in some cases was equivalent to a 10 degree angle difference between the programmed angles and the actual angle achieved. Further, the technique used to measure the panel angles added to the uncertainty. The angle that the photographs were taken at could change the measurement by approximately another 5 degrees. So the angles plotted have

an uncertainty of ± 5 degrees. Other uncertainties include the wind speed and atmospheric condition measurements.

4.2 Power Requirements

Another important aspect in the vehicle design is the power required to mechanize the wings. During the wind tunnel test, an external power source was hooked up to the vehicle; however, future iterations of the model will include an onboard power supply for the vehicle applications to be feasible. Therefore, tests were completed to determine the power and energy required to rotate the wings.

It was desired to complete the power requirement measurements during the wind tunnel testing in order to account for the added torque effects due to the pitching moment. However, during the wind tunnel tests measurements did not account for the voltage added to the system from the USB control computer. It was later discovered that the voltage from the control computer is not constant as suspected, but instead changes throughout the test. Therefore, it was necessary to complete benchtop tests to obtain results that include this added voltage from the controller. The results from the benchtop tests do not account for the torque due to the pitching moment; however, the pitching moment expected to act on the wings during flight was small compared the the torque capabilities of the servo motors and it was decided that benchtop tests would be adequate to determine the approximate power required to actuate the wings.

4.2.1 Circuit

In order to determine the total power that was required to mechanize the model, both the voltage and the current must be known. The data acquisition system used was not capable of measuring current; therefore, resistors were incorporated into the existing circuit.

By measuring the voltage across the known resistors, the current could be calculated. The circuit used for testing is shown in Figure 4.12. Voltages were measured at the small circle locations. A Y-harness, as shown in Figure 4.13, was used to separate the voltage from the control chip. The theory of the Y-harness states that each end of the Y will see the same voltage. During the testing one end of the y-harness was used for voltage measurement and the motor was connected to the other end. The resistors, previously mentioned, were added to the circuit in series with the motor for current calculations. During the test, the voltage into each motor from the power supply (red to black wire measurement), voltage into each motor from the control computer (yellow to black measurement), and the voltage across each resistor were measured. Once the total voltage into the motor and the current were known the motor power was calculated using Equation 4.3.

$$P_M = \left(\frac{V_R}{R} \right)^2 \left(\frac{RV}{V_R} - R \right) \quad (4.3)$$

Where V_R is the voltage measured across the resistor, R is the resistance, in this case 1 Ohm, and V is the total voltage into the motor. This voltage includes the voltage from the power supply, and the additional voltage V_o from the USB cord to control the motors. The V_o value that was measured from the USB cord used to control the motor movement was a square wave impulse with an amplitude of 5 volts. The length of the impulse was approximately 2 ms with a frequency of 50 cycles per second. The impulse length is what actually varied with the different motor positions.

4.2.2 Benchtop Test Setup

Figure 4.14 shows the test setup for the benchtop power tests. The same circuit was used for both the wind tunnel test and the benchtop power tests. The difference was in how the measurements were made. During the wind tunnel tests only the voltage into the proximal motor from the power supply and the voltage across the resistor were

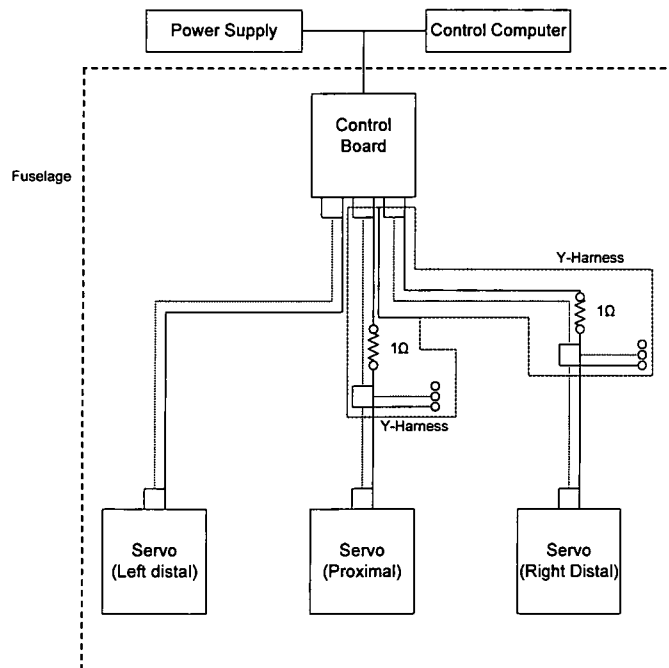


Figure 4.12: Power Measurement Circuit

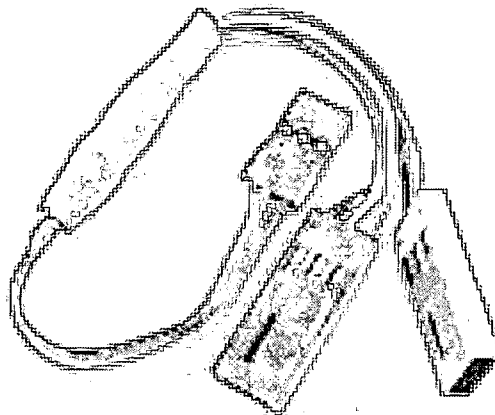


Figure 4.13: Y-Harness

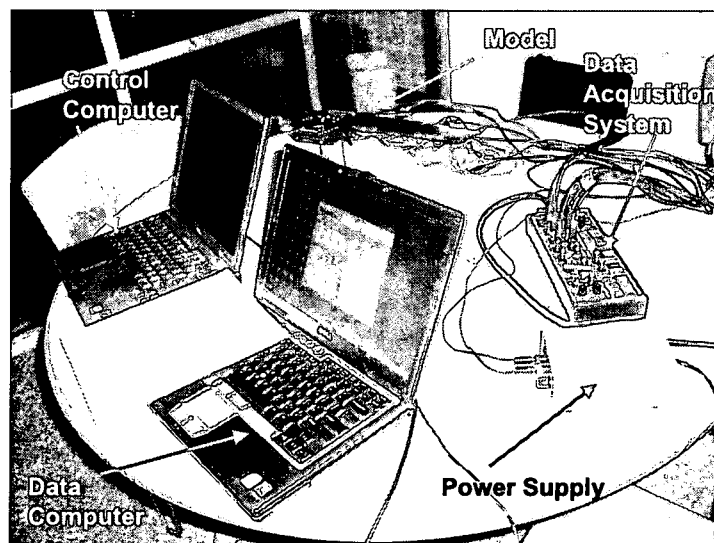


Figure 4.14: Benchtop Power Test Setup

measured. During the benchtop tests both of these were measured including the voltage into the system from the USB cord. Two computers were used, one to control the wings and a second to record the voltage data. The model was hooked up to a power supply set to deliver 4.5 volts. A data acquisition system with 6 channels was used to measure the power required to drive the proximal motor and one distal motor. Measurements taken include power into each motor from the power supply and from the USB controller as well as the voltage across the resistors.

4.2.3 Results

Before the tests were completed, specifications about the distal servo motors were used to approximate the amount of power that would be needed to rotate the wings. The distal motors had a voltage recommendation of 4.8 to 6 V. However, for the testing the power supply accessible had an available voltage of 4.5 V. This voltage seemed to be enough to properly drive the motors. The specifications also stated that the distal motors had an average current rating of 100 mA with a maximum of 300 mA and a static rating of 1 mA. Using this data the average power was calculated to be 0.45 W with a maximum at 1.44 W and a static power of 0.0045 W. Similar specifications for the proximal servo motor could not be obtained. Since the proximal motor is slightly larger than the distal motors and is used to rotate both proximal panels, it was assumed that it would require more power and was focused on during the power testing.

Figure 4.15 shows the instantaneous power as a function of time for a proximal wing rotation from 0 degrees wing incidence to 85 degrees. In this test, the peak instantaneous power was found to be 0.50 W with a static power of approximately 0.1 W. This result is typical of the power measurements for most tests. A very small amount of power is required to maintain the wing in a static position. As the motor moves the wing into position the

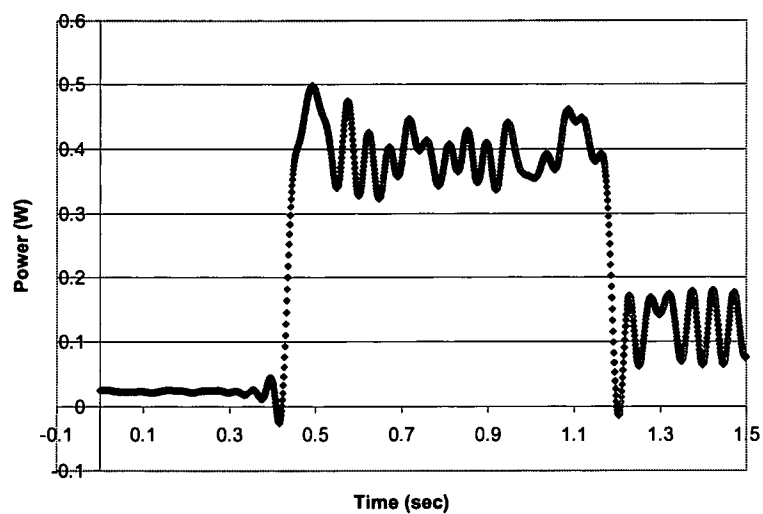


Figure 4.15: Power Results for Proximal Wing Rotation from 0 to 85 Degrees

power increases to a higher level and remains at this level during the entire motion. After the motion is completed, the power is reduced to the static level.

The benchtop tests were repeated 5 times. The average power and standard deviation were calculated for each different angle rotation. Figures 4.16, 4.17, 4.18, 4.19, and 4.20 show the test results for instantaneous power for several tests. These results are representative of the rest of the results. The results for all of the tests are summarized in Table 4.7. The average peak power results are summarized in Table 4.8.

There does not seem to be significant trends between the maximum instantaneous power and the angle rotation, only between the positive rotation and negative rotation. A higher peak power was found during the negative rotation tests compared to the positive rotation tests. Since the motors are attached to spars at the quarter chord of the wing, the mass distribution could be the cause of the different power required for positive rotation compared to negative rotation. During a loaded condition, the aerodynamic pitching moment would help the motors rotate the wings during the positive angle rotation and would reduce the power necessary for the motion. The pitching moment would work against the motors for the negative rotation.

4.2.4 Energy Requirements

To obtain an approximation of the energy required to mechanize the wings, a generic mission scenario of a 20 min flight with a 20 sec landing was used. Assuming no movement for the flight and an average of 0.35 W during landing resulted in an energy of 381 J. This is the low end of the power required. For a 20 min flight with constant wing moment, the resultant energy was 1281 J. These energy values are very reasonable. As a comparison, a rechargeable AAA Nickel-Metal Hydride (NiMH) battery is capable of supplying 1.2 Volts and 850 mAh and weighs 13 g. A set of four of these batteries could power the vehicle with 4.8 V for approximately 16.3 hours weighting 52 g. This power source may be too

Table 4.7: Power Test Results

Test Number	Angle Start	Angle End	Static Power Start	Peak Power	Power During Motion	Static Power End
	Deg	Deg	Watt	Watt	Watt	Watt
1	0	10	0.10	0.56	0.32	0.09
2	0	10	0.04	0.51	0.21	0.06
3	0	10	0.09	0.58	0.31	0.08
4	0	10	0.07	0.58	0.30	0.09
5	0	10	0.03	0.50	0.30	0.09
Average			0.07	0.55	0.29	0.08
Standard Deviation			<i>0.03</i>	<i>0.04</i>	<i>0.05</i>	<i>0.01</i>
1	0	45	0.09	0.51	0.34	0.04
2	0	45	0.02	0.53	0.35	0.10
3	0	45	0.06	0.52	0.35	0.09
4	0	45	0.04	0.54	0.36	0.09
5	0	45	0.02	0.57	0.32	0.06
Average			0.05	0.54	0.34	0.07
Standard Deviation			<i>0.03</i>	<i>0.02</i>	<i>0.01</i>	<i>0.03</i>
1	0	85	0.11	0.53	0.35	0.10
2	0	85	0.02	0.57	0.38	0.14
3	0	85	0.08	0.52	0.40	0.12
4	0	85	0.04	0.61	0.39	0.12
5	0	85	0.02	0.50	0.38	0.12
Average			0.06	0.54	0.38	0.12
Standard Deviation			<i>0.04</i>	<i>0.04</i>	<i>0.02</i>	<i>0.01</i>
1	10	0	0.02	0.69	0.45	0.11
2	10	0	0.02	0.64	0.35	0.02
3	10	0	0.02	0.64	0.43	0.19
4	10	0	0.02	0.62	0.41	0.15
5	10	0	0.02	0.59	0.42	0.17
Average			0.02	0.64	0.41	0.13
Standard Deviation			<i>0.00</i>	<i>0.04</i>	<i>0.04</i>	<i>0.07</i>
1	45	0	0.01	0.18	0.11	0.03
2	45	0	0.02	0.63	0.45	0.17
3	45	0	0.02	0.72	0.46	0.18
4	45	0	0.02	0.62	0.45	0.16
5	45	0	0.02	0.70	0.47	0.18
Average			0.02	0.67	0.39	0.15
Standard Deviation			<i>0.01</i>	<i>0.22</i>	<i>0.15</i>	<i>0.06</i>
1	85	0	0.09	0.74	0.48	0.15
2	85	0	0.02	0.63	0.51	0.09
3	85	0	0.02	0.69	0.50	0.15
4	85	0	0.02	0.75	0.49	0.26
5	85	0	0.02	0.65	0.50	0.14
Average			0.04	0.69	0.50	0.16
Standard Deviation			<i>0.03</i>	<i>0.05</i>	<i>0.01</i>	<i>0.07</i>

Table 4.8: Power Test Results- Averages

Angle Start	Angle End	Peak
Deg	Deg	Watt
0	10	0.55
0	45	0.54
0	85	0.54
10	0	0.64
45	0	0.67
85	0	0.69

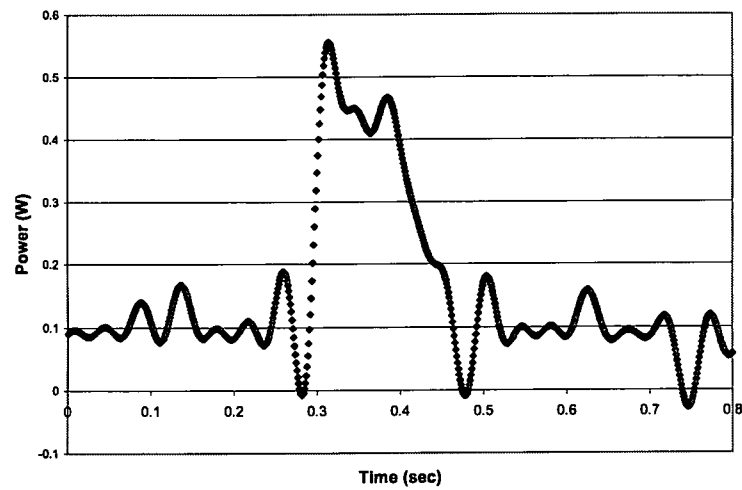


Figure 4.16: Power: Rotation of Proximal Wing From 0 Degrees to 10 Degrees

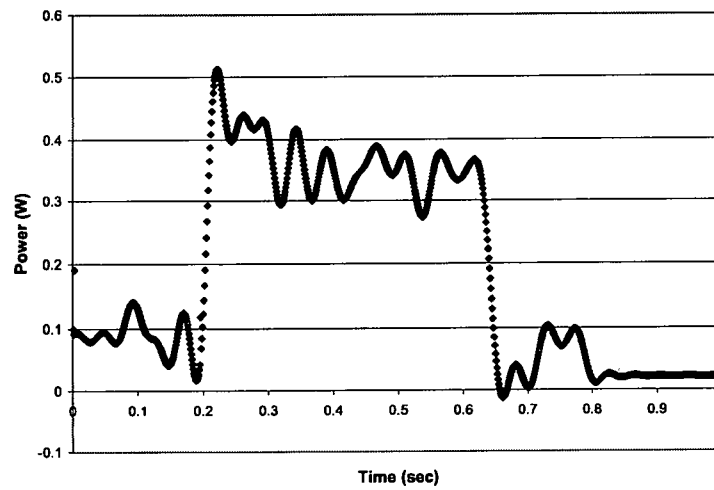


Figure 4.17: Power: Rotation of Proximal Wing From 0 Degrees to 45 Degrees

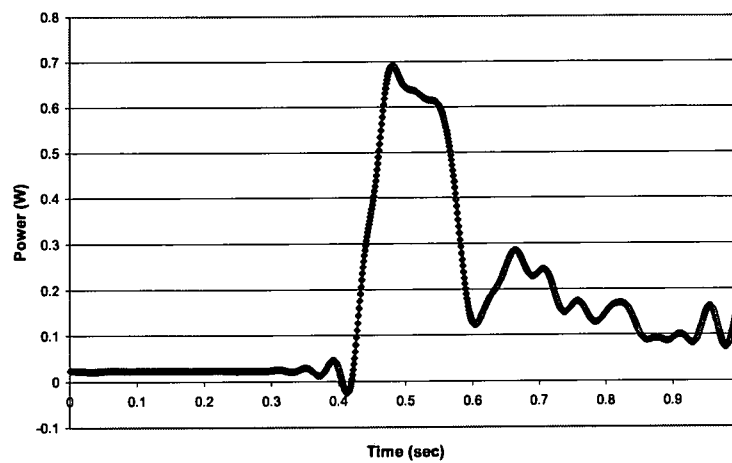


Figure 4.18: Power: Rotation of Proximal Wing From 10 Degrees to 0 Degrees

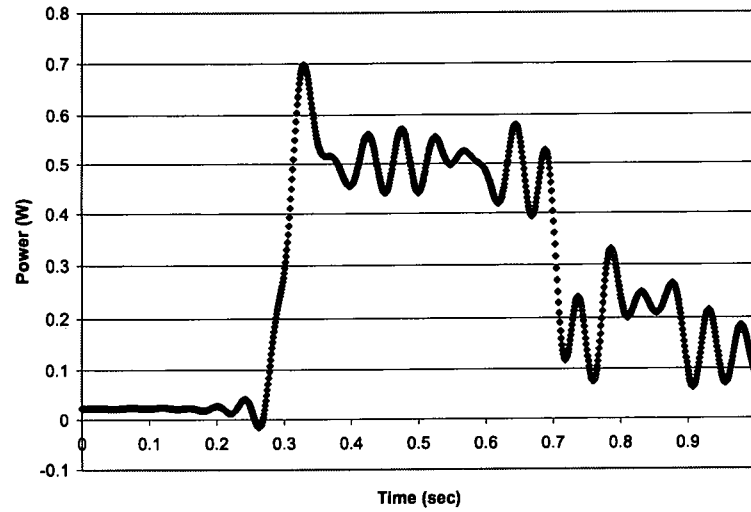


Figure 4.19: Power: Rotation of Proximal Wing From 45 Degrees to 0 Degrees

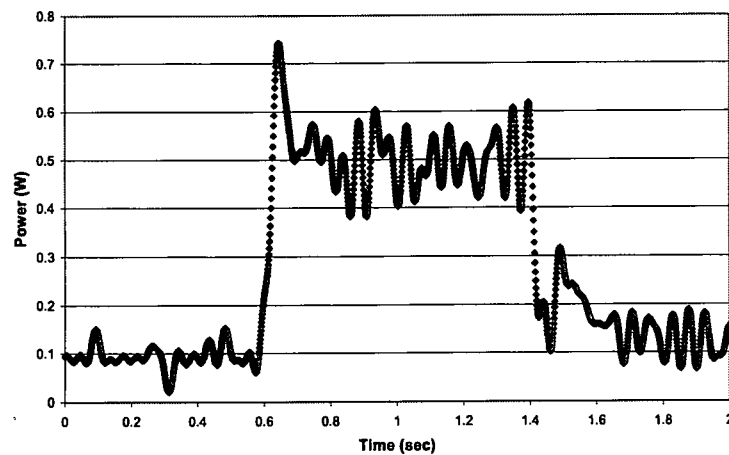


Figure 4.20: Power: Rotation of Proximal Wing From 85 Degrees to 0 Degrees

massive for this size vehicle; however, it helps approximate the battery size necessary for wing mechanization.

Utilizing the power data along with possible mission scenarios for the vehicle could help determine the power and energy required for other notional vehicle missions. Once power and energy requirements are determined, a power source can be selected and energy harvesting techniques can be investigated [16].

Chapter 5

Analytical Model

An integrated aeroelastic multi-body morphing simulation tool called IAMMS was used to analytically model the MAV and to simulate the vehicle in flight [41]. The results from the model simulations were compared to wind tunnel test results, and were used to obtain analytically based values for the aerodynamic and structural forces acting on the vehicle. The analytical model serves as an estimate of the forces that can be expected to act on the vehicle during a landing trajectory. For future research, the analytical model can be used to further develop the vehicle to optimize the landing trajectory and vehicle design and to investigate control schemes for perching.

5.0.5 Analysis Tool

IAMMS utilizes the multi-body dynamics code MSC-ADAMS and, therefore models are built inside the ADAMS environment. The ADAMS solver is used to perform time integration for the multi-body model of the vehicle. The loads are computed for each time step using an AFRL-developed code that utilizes vortex lattice computations and splining techniques to interpolate the aerodynamic forces to the structure [41]. Matlab/SIMULINK is used for the flight control system. For the present study no flight control system was used. Instead, the simulations consisted of commanded motions corresponding to wind tunnel tests.

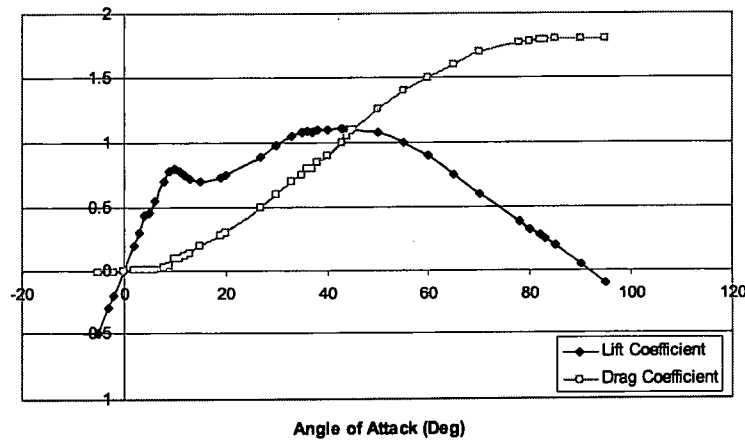


Figure 5.1: Lift and Drag Coefficient Splines

The original aerodynamic code used to determine the loads acting on the model did not take into consideration post stall events. Because in many cases portions of the wings in the model will be at angles beyond stall, additional calculations needed to be made for the post stall aerodynamics. To do this, post stall airfoil data was developed into two splines, one each for lift and drag coefficients, and was incorporated into the original tool. This data for the lift and drag coefficients is shown in Figure 5.1 and was obtained from wind turbine high angle of attack data [7]. The lift coefficient data specifies a stall point at 10 degrees corresponding to a lift coefficient of 0.8. After stall, at around 15 degrees, the lift coefficient starts to increase again. The maximum lift coefficient for this airfoil is at 45 degrees upon where the lift coefficient continues to decrease. The drag coefficient remains at a very low amount until after stall, at which time it increases basically as the sine of the angle of attack until it reaches a maximum of 90 degrees.

5.0.6 Simulation Model

In ADAMS the mechanized vehicle was structurally replicated to include the three spars and the wing ribs as shown in Figure 5.2 . A rectangular box shaped fuselage was

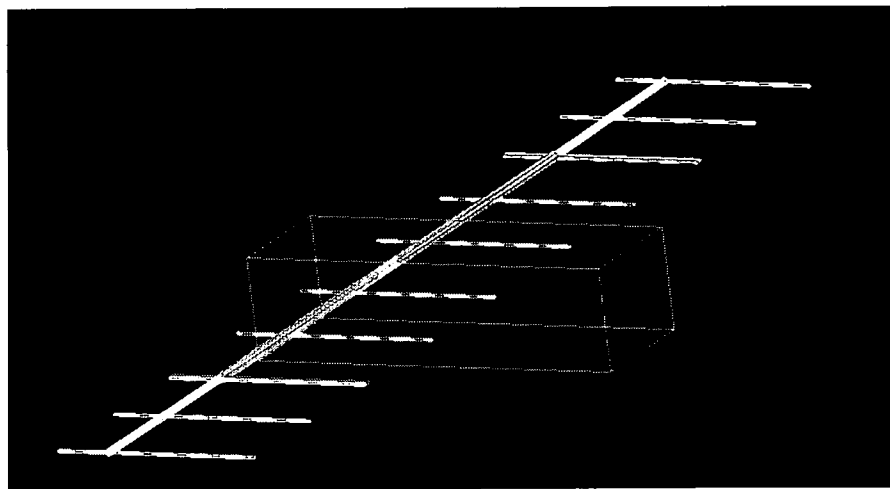


Figure 5.2: Analytical Model in ADAMS

included with the model and has its own aerodynamic grid. The fuselage in the physical model is a symmetrical airfoil at zero degrees angle of attack and therefore generates zero lift and negligible drag attributed only to skin friction.

The three spars in the model were built using bar elements and were linked together with revolute joints at inner ends of the distal spars to allow for only the torsional degree of freedom. To replicate the physical spars, the proximal spar in the model is a hollow circular cylinder that extends through the fuselage and the two distal spars are solid cylinders that fit within the proximal spar and end just inside the fuselage. The three spars were modeled to be completely independent of each other besides the connection at the distal spar inner ends. All three spars are capable of independent rotation.

Twelve ribs were included in the model with three ribs for each of the four wing sections in the physical model. The ribs serve as structural members and are clamped to the spars. Each rib has three applied force locations that were interpolated from the aerodynamic vortex lattice code. The three force locations are at the spar and on the two ends.

The aerodynamic model consists of four separate wing panels and paneling for the fuselage. The wing panel velocities for each test are defined by the center of gravity motion and are included as part of the boundary conditions for the vortex lattice solution. Four wing panels, modeled by the spars and ribs, can be programmed to rotate to any angle specified up to 90 degrees. The proximal wing, right distal wing, and left distal wing angles are controlled using wing angle splines attached to three state variables, one for each independent wing section. Separate splines were written to replicate each of the tests completed in the wind tunnel. The tests range in speeds, from 1 to 10 m/s, and in angle changes. The center of gravity motion was defined as the wind tunnel velocity for each test. The material properties used for this model are arbitrary because this model does not account for gravitational effects on the model, nor does it account for aeroelastic effects.

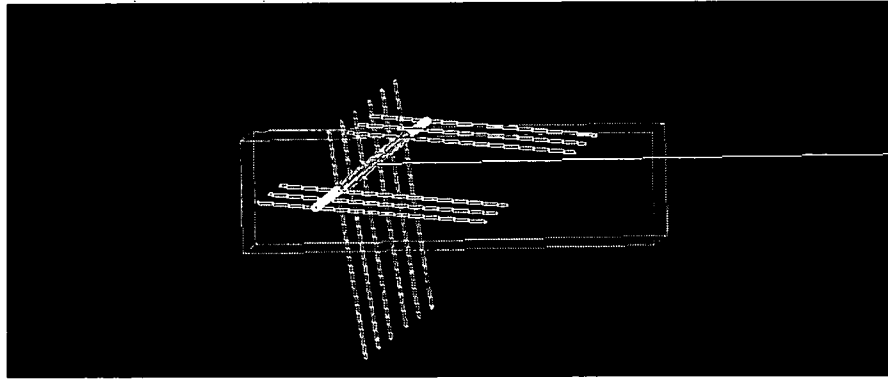


Figure 5.3: Analytical Model in ADAMS With Proximal Wing Sections at 82 Degrees and Distal Wing Sections at 6 Degrees.

Therefore any material could be selected for this rigid model.

Once the flight speed and wing angle splines for each wing section state variable were specified, a simulation was run to determine the torques and forces acting on the model. Figure 5.3 shows the model at the end of test 15. The white line represents the flight path during the simulation. In this tool, the model moves in space rather than the flow moving over the surface. During this test all the wing sections started at 2 degrees wing incidence. The distal wing sections (green ribs) rotated to 6 degrees wing incidence and the proximal wing sections (red ribs) rotated to 82 degrees wing incidence. This modeling of the wind tunnel tests is the same as the method used for large-scale morphing vehicle analysis [41].

5.0.7 Results

Several different wing incidence variations and wing speeds were simulated in ADAMS to determine the aerodynamic forces and moments acting on the model during an assumed flight trajectory. As the vortex lattice model used for pre-stall aero predictions cannot compute drag, zero drag is shown until after the assumed stall event. Figures 5.4, 5.5, 5.6, and

5.7 show the results for lift, drag, wing rotation, and proximal and distal torque as a function of time for several different simulations. For these simulations 100 time steps were used.

Figure 5.4 shows the results for test 17. In this test the flight speed was set to 5 m/s and only the distal wing was programmed to rotate; the proximal wing panels remained stationary at 83 degrees throughout the test. At the beginning of the simulation, the distal wing panels both started at 5 degrees and rotated linearly to 78 degrees. The results show a peak lift value near 45 degrees and an increasing drag through the stalled portion of the simulation. The maximum lift value was found to be approximately 0.6 N, the lift was also found to be nearly the same at the beginning of the test and at the end due to the similarity in lift coefficient at 5 degrees and 78 degrees. A sharp increase in the distal wing torque is evident at approximately 23 degrees where there is also an increase in drag.

Also simulated was test 22 as shown in Figure 5.5. In this test the flight speed was 7.5 m/s. Again, in this test only the distal wing panels rotated; the proximal panels remained at a wing incidence of 40 degrees throughout the simulation. At the beginning of the simulation, the distal wing incidence was 4 degrees. The distal panels rotated throughout the test and ended at 30 degrees. The lift increased throughout the test, and since the wing incidence never reached 45 degrees, the maximum lift was not obtained. An increase in both drag and torque is evident at a distal wing angle of approximately 17 degrees.

Figure 5.6 shows the results from test 25. In this test the flight speed was set to 10 m/s and all the wing sections moved during the simulation. The proximal wing sections started at 0 degrees and rotated to 5 degrees. The distal wing sections started at -3 degrees wing incidence and rotated to 10 degrees. The results show a zero drag throughout the entire test since none of the panels reach stall during the simulation. The lift increases throughout the test. The torque decreases throughout the test. The spikes in the torque are related to the modeling and do not correspond to actual events. Some model improvements made need to be completed to remove these peaks.

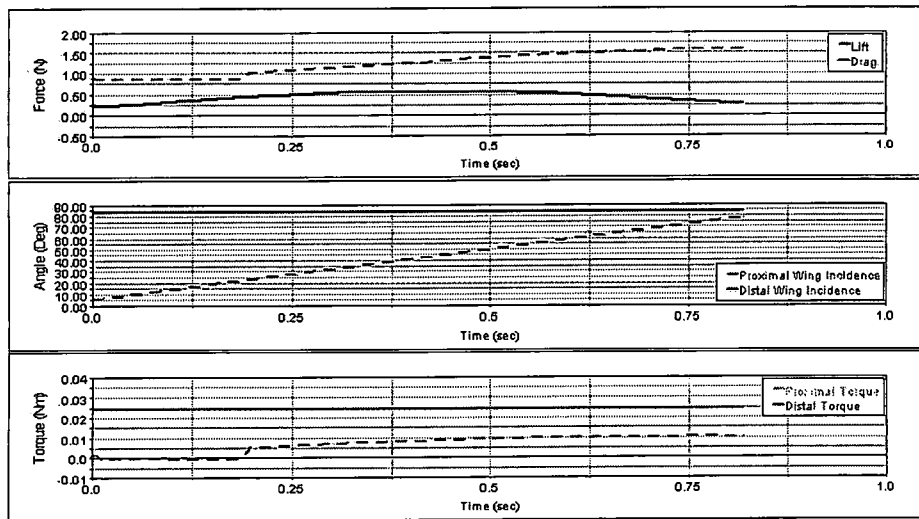


Figure 5.4: Analytical Lift, Drag, and Pitching Moment Results for Test 17

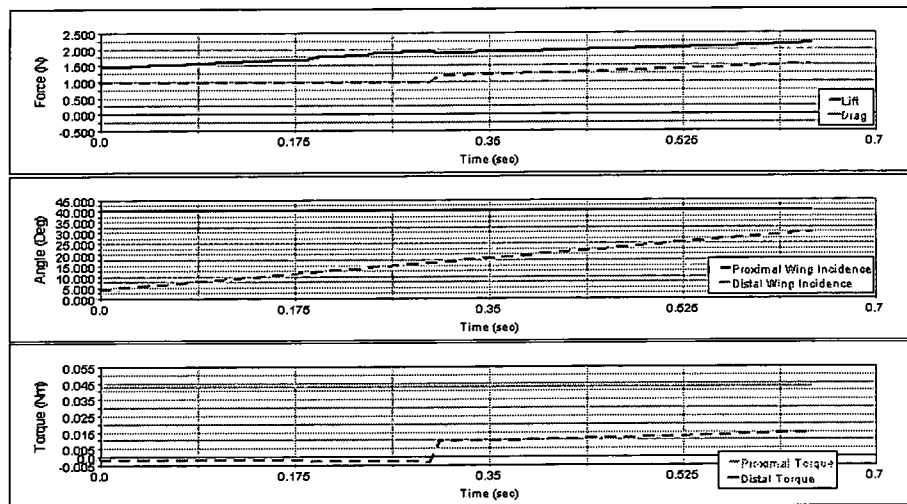


Figure 5.5: Analytical Lift, Drag, and Pitching Moment Results for Test 22

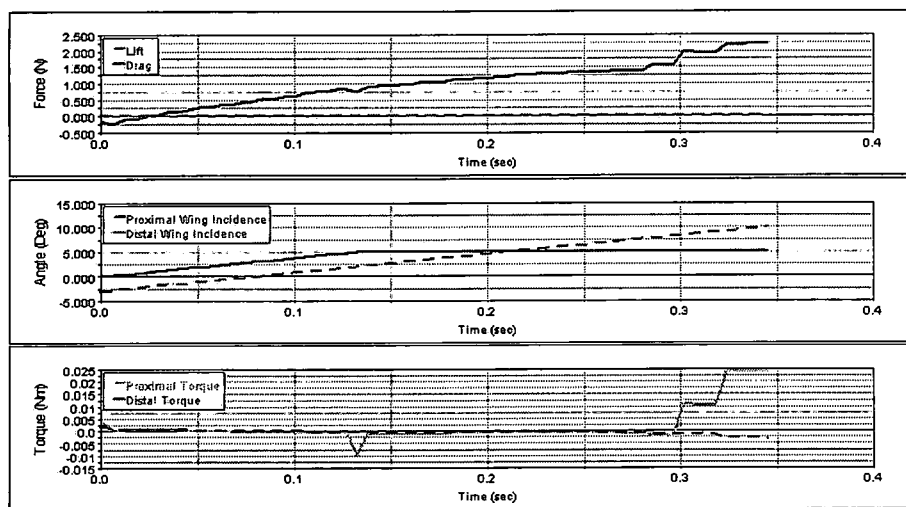


Figure 5.6: Analytical Lift, Drag, and Pitching Moment Results for Test 25

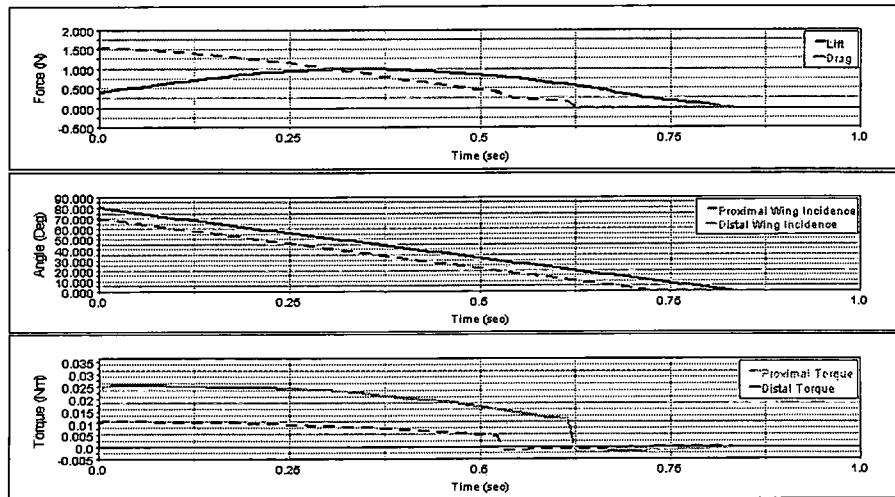


Figure 5.7: Analytical Lift, Drag, and Pitching Moment Results for Test 29

The last test examined is shown in Figure 5.7. In this simulation, corresponding to test 29, the flight speed was set to 5 m/s. During the simulation, the proximal sections started with a wing incidence of 80 degrees and the distal panels started with a wing incidence of 70 degrees. All the panels rotated until they reached 0 degrees. In the test a maximum lift of approximately 0.9 N is achieved when the proximal wing panels are at 45 degrees. After this point, the lift decreases. Two dips in the drag and panel torque are evident when each panel stalls.

Another run was completed in IAMMS to determine the lift, drag, and pitching moment acting on the model when all wing panels began at 0 degrees and rotated to 25 degrees with a flight speed of 10 m/s. This was completed to verify that there was adequate lift available for cruise at 10 m/s. These results are shown in Figure 5.8. In this test, an adequate lift is obtained at approximately 14 degrees. Also in this test, two lift peaks are evident. One lift peak occurs at stall, at which point the lift declines, but then increases again throughout the tests as expected from the quasi-steady results. At a flight speed of 10 m/s with all wings positioned at 14 degrees incidence, there is more than enough

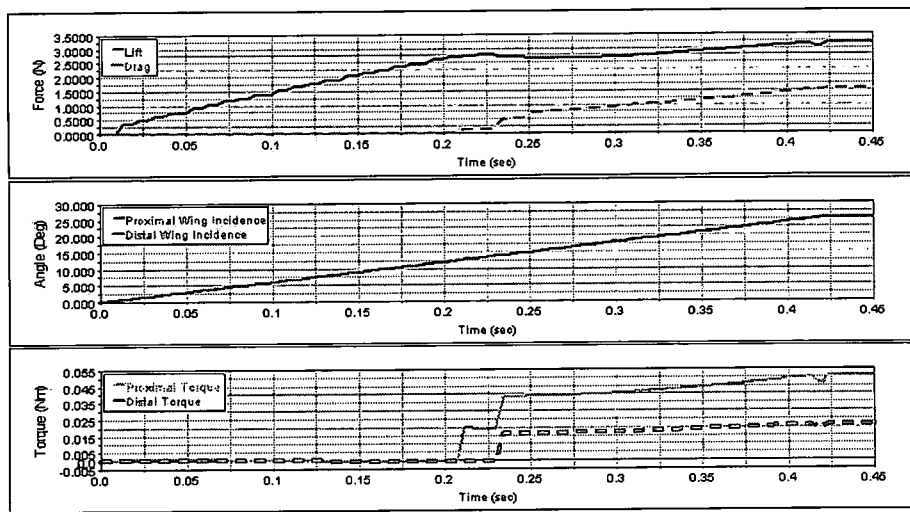


Figure 5.8: Analytical Lift, Drag, and Pitching Moment Results for Full Wing Rotation from 0 to 25 Degrees at 10 m/s

lift to sustain flight for the vehicle; however, the lift observed in the previously described runs is lower than the lift required to maintain steady level flight for the 306 g vehicle. It should be noted that this model assumes a symmetric airfoil and does not include dynamic effects. As observed in wind tunnel tests, dynamic effects may create an added lift when the wing panels are quickly rotated. Using a high lift cambered airfoil would also increase the vehicle lift and its ability to perform a perched landing. Accounting for dynamic effects and changing the wing airfoil would improve the model.

Several other simulations were completed to further develop the model, the results for these test can be found in the appendix. In all the simulations a specified flight speed was set for the entire wing rotation. In future simulations, the flight speed will be programmed to vary as the wings rotate. This type of modification will allow for trajectory approximation and eventually lead to determining the wing section rotations that correspond to an optimized landing trajectory. Other data available from the IAMMS simulation includes actuator torques. If a completed servo system and four-bar linkage was included, then actual power measurements could also be made. Additionally, once a free-flying model is developed, IAMMS will be able to simulate the controlled flight using a flight control system.

Although the lift results for the described runs are slightly lower than necessary for sustained flight, these results do not represent an optimized condition for perching. Analyzing multiple landing trajectories and wing rotation speeds would assist in determining an optimized maneuver. A possible landing trajectory for this vehicle may include an ascending trajectory toward the end of the flight path that utilizes dynamic stall effects to increase lift and pull the vehicle upwards to perch on its landing target. Another possible landing solution requires the vehicle to glide toward the landing target while increasing wing angle to increase drag. Several possibly landing trajectories are shown in Figure 5.9. The colored lines represent different paths that the vehicle could take upon landing. Further analysis

should be completed for model improvement and landing trajectory optimization.

5.0.8 Comparison to Wind Tunnel Results

The results from the analytical model were compared to the wind tunnel results and it was found that the wind tunnel results were significantly different. As previously mentioned, there were several uncertainties in the wind tunnel testing including inaccurate calibration techniques. Therefore, the analytical results cannot be absolutely validated based on this set of results. The compared results do show similar trends between the wind tunnel forces and the analytical forces. However, the analytical model did not account for dynamic effects, and it used assumed values for lift coefficient and drag coefficient for post stall angles. Therefore in the analytical model the results for lift did not begin to decrease until 45 degrees. For example, Figure 5.10 shows a comparison of the analytical model and the wind tunnel results for test 29. In this test the proximal wings started at 80 degrees and rotated to 0 degrees and the distal wings started at 70 degrees and rotated to 0 degrees. Notice that the lift curves are similar in shape, however the analytical results show a higher maximum lift value and an earlier maximum lift than the wind tunnel tests. The analytical results show a maximum lift at proximal wing incidence of 45 degrees and the wind tunnel results show a maximum lift at a proximal wing incidence of 41 degrees. Figure 5.11 shows another comparison between wind tunnel test results and analytical model results. Again, similar trends are evident in both tests; however, the values are slightly different. Further tests should be completed with reduce experimental uncertainty. These results could be incorporated into the analytical model for more accurate dynamic effect simulations.

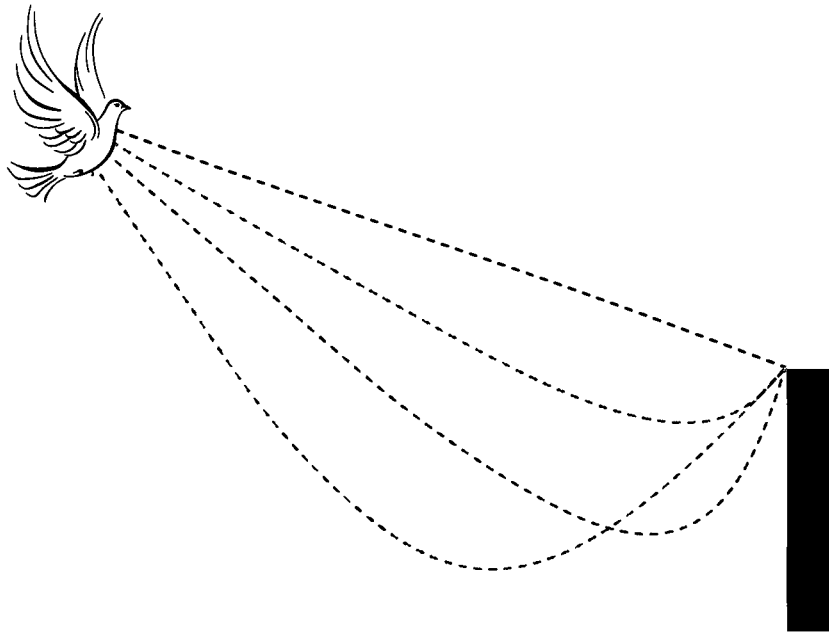
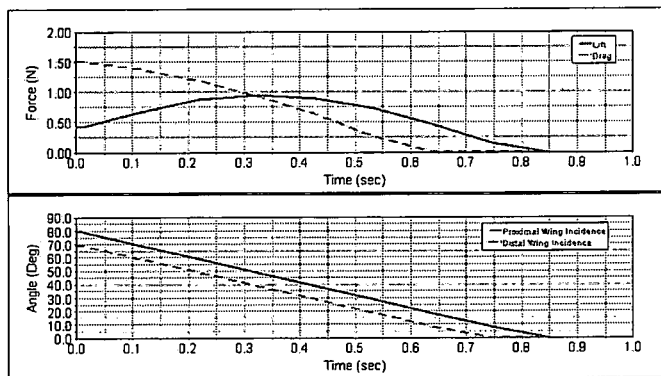


Figure 5.9: Possible Perching Trajectories



a.)

b.)

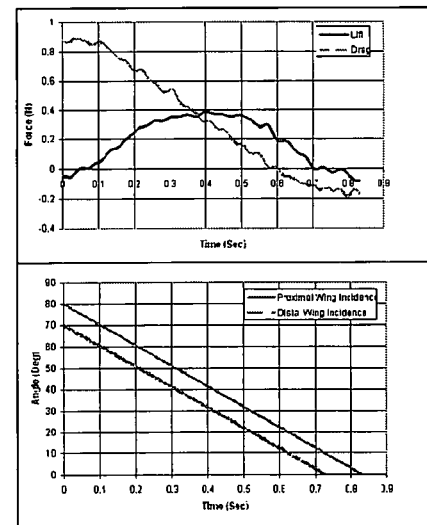


Figure 5.10: Comparison of Wind Tunnel and Analytical Results for Test 29 a.)Analytical Model Results b.)Wind Tunnel Results

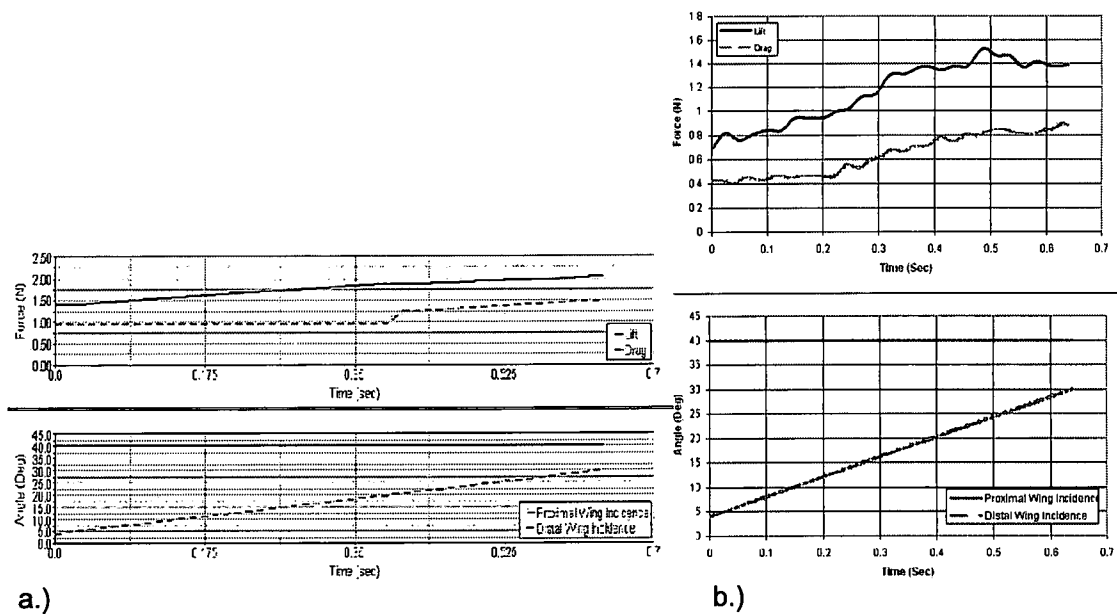


Figure 5.11: Comparison of Wind Tunnel and Analytical Results for Test 22 a.)Analytical Model Results b.)Wind Tunnel Results

Chapter 6

Conclusions and Recommendations

6.1 Conclusions

The goal of this project was to determine if a vehicle could be built that was light weight, structurally robust, and could develop the forces required to perform a perching maneuver using only wing deflections, inspired by bird landing techniques. The model constructed is a first iteration at developing such a vehicle and was successful in withstanding the assumed landing trajectory forces. The model met all size and weight requirements. Although much additional design work needs to be completed, such as adding a tail and developing control strategies among others, this first iteration vehicle achieves its desired result.

Wind tunnel testing was completed to determine two things. First it was important to determine if the model was structurally robust enough and the actuation was powerful enough to withstand the forces that it would encounter during an assumed flight trajectory, including forces related to flutter and dynamic effects. During the wind tunnel test, there were some wing vibrations noticed in the distal wings, but the actuation and structure met their requirements during testing. Secondly, the test was meant to develop an understanding of the order of magnitude of the forces that could be expected during wing rotations and the approximate power required to rotate the wing panels during flight. It also served as a dry run for further tunnel testing. The analytical model coupled with the wind tunnel results

showed that some dynamic effects are taking place during the wing rotation. These effects can be better understood with more wind tunnel tests and more accurate measurements techniques including flow visualization. Power measurements were taken for the proximal wing actuators. These measurements did provide a starting point for required power approximation. More testing should be completed to determine the actual power required for a full flight.

6.2 Recommendations

In future tests, more accurate methods for calibrating the sensor and for determining tunnel speed and wing angle will be utilized. Also, a tunnel designed to operate at very low speeds, on the order of 1 m/s, will be used for testing. Analysis is currently being completed to analytically understand the forces that act on the model during flight. A simulation model has been constructed using IAMMS to better understand the forces acting on the structure of the model and to help develop trajectories for the perching maneuver.

Completing tests at the REEF (Research and Education Engineering Facility) wind tunnel at the University of Florida would be extremely beneficial to this project. This open-jet open-test section enclosed tunnel is capable of variable speeds which would allow for trajectory simulations. Utilizing this facility for a future wind tunnel test would improve upon the previous tests completed. Other capabilities that the REEF tunnel has includes the ability for more accurate wing incidence angle measurements as well as flow visualization techniques.

Further wind tunnel tests would also allow for more accurate power measurements. For this project, voltages were measured separately from the load cell force measurements. Linking the two data acquisition systems, or creating one system to measure all the data, would allow for syncretization of the data. Also, during this project four voltages

were measured during the wind tunnel tests, two for each motor (proximal and one distal motor). Due to the circuitry used for the power measurements, the total power was not obtainable from the wind tunnel results. Instead, benchtop tests were completed to determine the actual power. Although the benchtop tests did provide a order of magnitude of power that would be necessary, actual power measurements should be completed during wind tunnel testing to account for the added torque generated by the pitching moment acting on the wing during flight. In order to achieve these measurements, some changes need to be made to the wind tunnel power tests. One additional voltage could be measured for each motor to account for the voltage into the system from the USB cord. The additional measurement could be made as completed during the benchtop test. This would require a measurement across the resistor, a measurement from the red to black wires on the free end of the Y-harness, and a measurement from the yellow to black wire on the free end of the Y-harness.

6.3 Summary

This model is a first iteration at developing a mechanized, bird-like, vehicle capable of a perching maneuver. Future models will need added degrees of freedom in the wings, as well as a mechanized tail and built in energy harvesting techniques. Eventually, the model should mimic bird-like behavior and should contain onboard cameras and communication devices. This model was successful in understanding the effects of wing rotational motion and the power necessary for a perching maneuver.

Appendix A

Mount Design

A mounting fixture was designed specifically for this application. The drawings for the mount are given in this section.

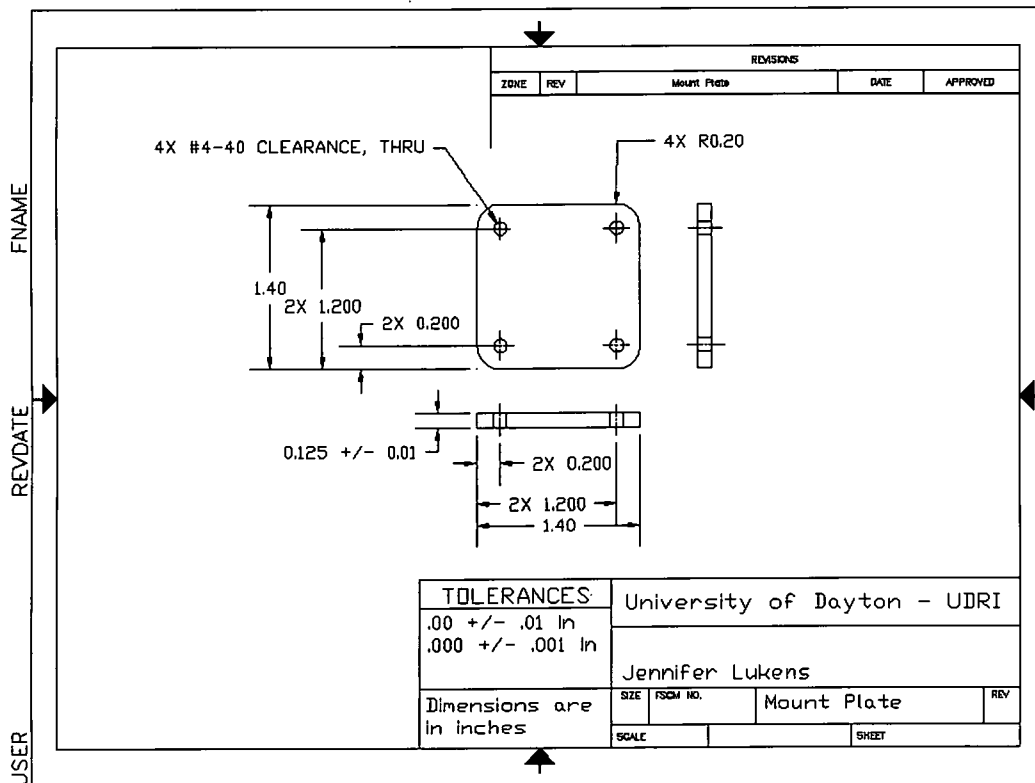


Figure A.1: Mount Plate

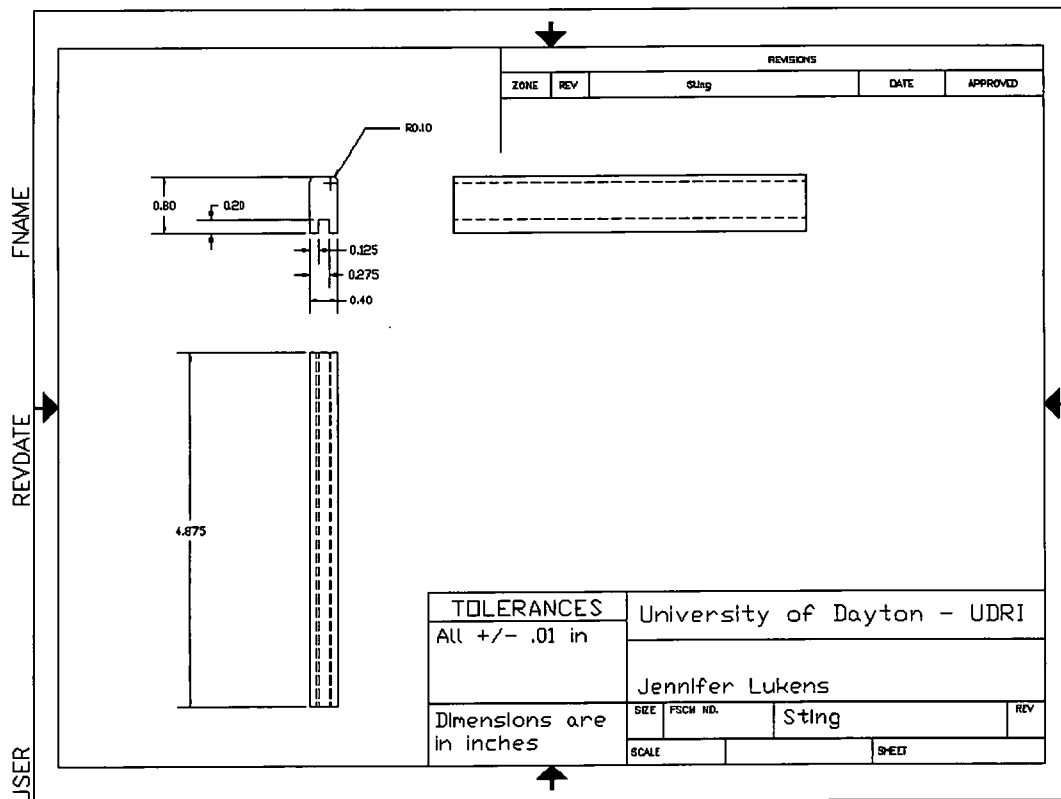


Figure A.2: Sting

FNAME		REVDATE		USER																											
<table border="1" style="width: 100%; border-collapse: collapse;"> <thead> <tr> <th colspan="4" style="text-align: center;">REVISIONS</th> </tr> <tr> <th style="width: 10%;">ZONE</th> <th style="width: 10%;">REV</th> <th style="width: 50%;">Base Plate</th> <th style="width: 10%;">DATE</th> <th style="width: 10%;">APPROVED</th> </tr> </thead> <tbody> <tr> <td colspan="5" style="height: 40px;"> </td> </tr> </tbody> </table>						REVISIONS				ZONE	REV	Base Plate	DATE	APPROVED																	
REVISIONS																															
ZONE	REV	Base Plate	DATE	APPROVED																											
<table border="1" style="width: 100%; border-collapse: collapse;"> <thead> <tr> <th colspan="2" style="text-align: center;">TOLERANCES</th> <th colspan="4" style="text-align: center;">University of Dayton - UDRI</th> </tr> </thead> <tbody> <tr> <td colspan="2" style="text-align: center;">.00 +/- .01 in</td> <td colspan="4" rowspan="2" style="text-align: center; vertical-align: middle;">Jennifer Lukens</td> </tr> <tr> <td colspan="2" style="text-align: center;">.000 +/- .001 in</td> </tr> <tr> <td colspan="2" style="text-align: center;">Dimensions are in Inches</td> <td style="width: 10%;">SIZE</td> <td style="width: 10%;">FSCM NO.</td> <td style="width: 50%;">Base Plate</td> <td style="width: 10%;">REV</td> </tr> <tr> <td colspan="2"></td> <td colspan="2" style="text-align: center;">SCALE</td> <td colspan="2" style="text-align: center;">SHEET</td> </tr> </tbody> </table>						TOLERANCES		University of Dayton - UDRI				.00 +/- .01 in		Jennifer Lukens				.000 +/- .001 in		Dimensions are in Inches		SIZE	FSCM NO.	Base Plate	REV			SCALE		SHEET	
TOLERANCES		University of Dayton - UDRI																													
.00 +/- .01 in		Jennifer Lukens																													
.000 +/- .001 in																															
Dimensions are in Inches		SIZE	FSCM NO.	Base Plate	REV																										
		SCALE		SHEET																											

Figure A.3: Base Plate

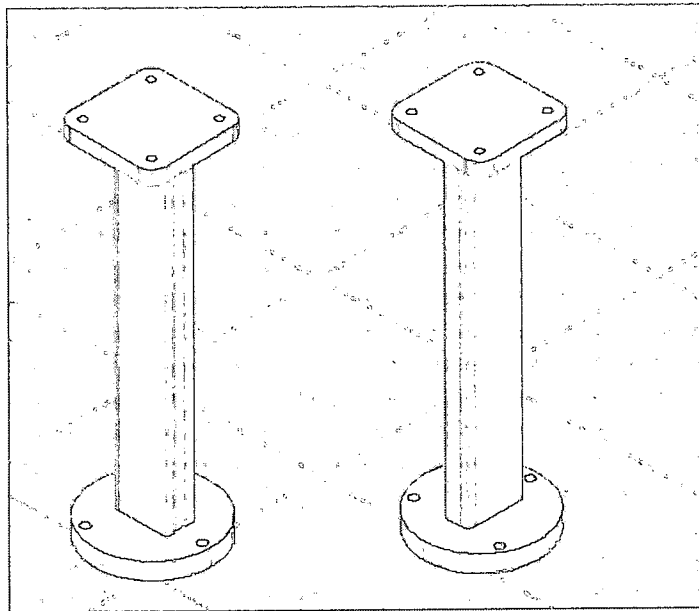


Figure A.4: Mount Assembly: Two Views

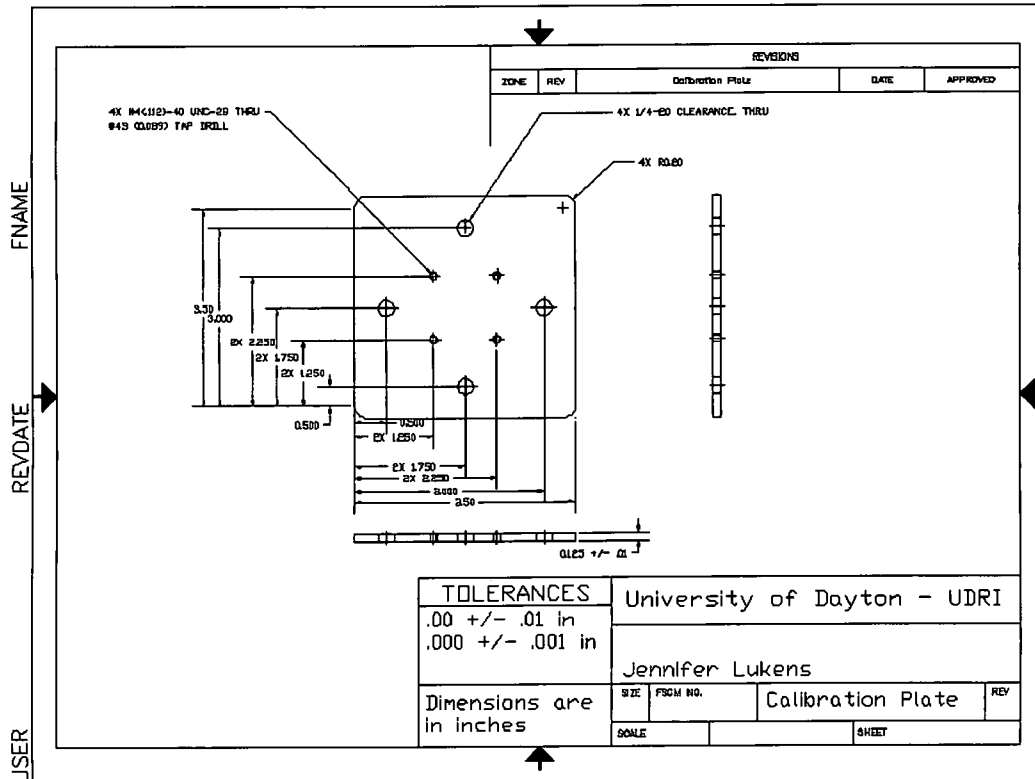


Figure A.5: Calibration Plate

Appendix B

Calibration Curves

The calibration curves used to generate the calibration matrix are provided below.

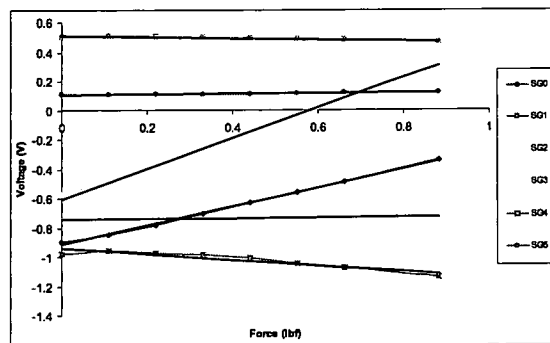


Figure B.1: Calibration Curves: Lift

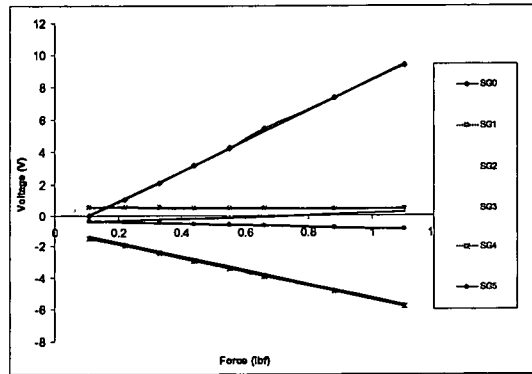


Figure B.2: Calibration Curves: Drag

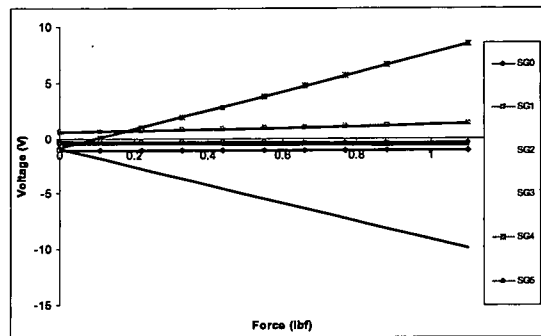


Figure B.3: Calibration Curves: Side Force

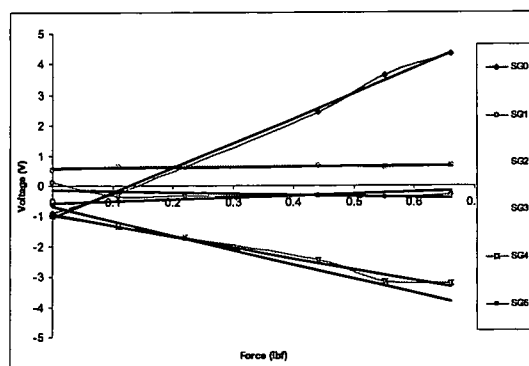


Figure B.4: Calibration Curves: Positive Pitching Moment

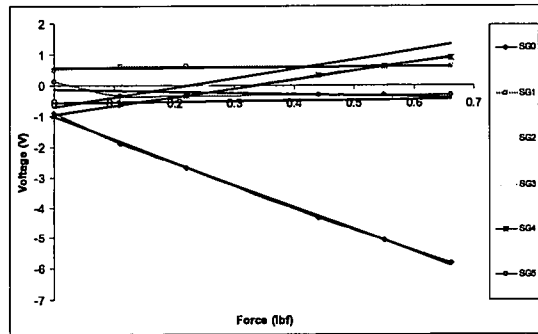


Figure B.5: Calibration Curves: Negative Pitching Moment

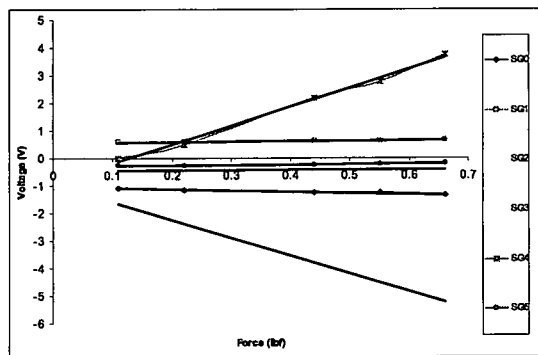


Figure B.6: Calibration Curves: Positive Rolling Moment

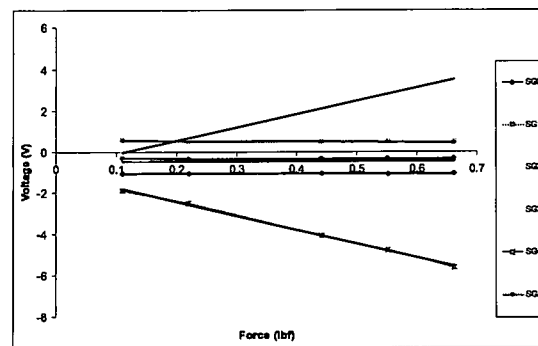


Figure B.7: Calibration Curves: Negative Rolling Moment

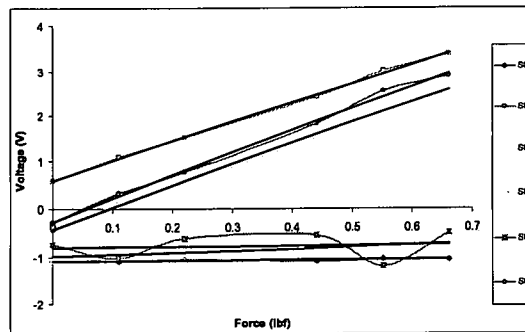


Figure B.8: Calibration Curves: Positive Yawing Moment

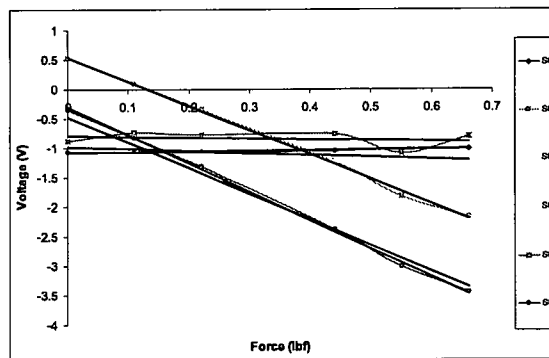


Figure B.9: Calibration Curves: Negative Yawing Moment

Appendix C

Wind Tunnel Results

Several wind tunnel tests were completed besides those analyzed in this paper. The results for the remainder of the wind tunnel tests completed are provided in this section.

In test 17, results shown in Figure C.1, the wind tunnel speed was set to approximately 5 m/s and the proximal panels were programmed to start at 85 degrees and remain at 85 degrees throughout the test. The distal wings were programmed to start at 10 degrees and rotate to 85 degrees during the test. However, the actual angles were found from photographs to be slightly different. The proximal wings were actually positioned at 83 degrees throughout the test and the distal wing panels started at 5 degrees and finished at 78 degrees.

In test 25 the tunnel speed was set to approximately 10 m/s and all wing panels were programmed to begin at 0 degrees and rotated together to 10 degrees. Instead, photographs showed that the proximal wing panels did begin at 0 degrees, but only rotated to 5 degrees. Also, the distal wing panels actually started slightly negative, at -3 degrees but did end at 10 degrees. Figure C.2 shows the lift and drag data during the rotational part of this test.

In test 28, results shown in Figure C.3, the wind tunnel speed was set to 5 m/s and the proximal and distal wing portions were all programmed to move from 45 degrees to 0 degrees. Photographs later showed that the proximal wing sections actually moved

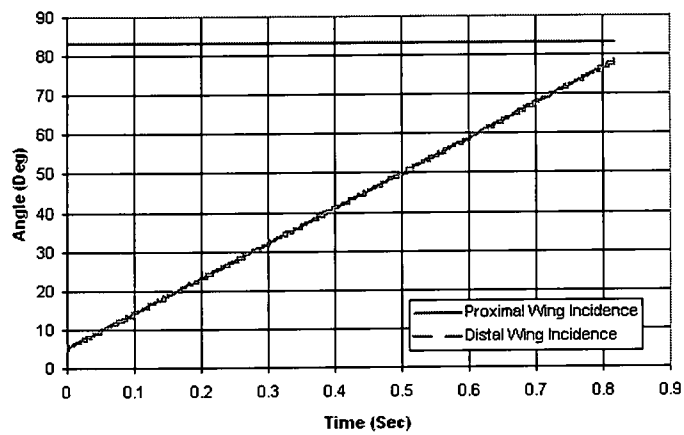
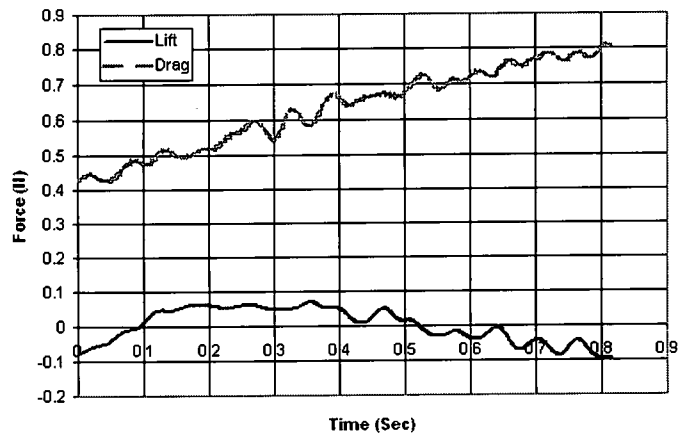


Figure C.1: Lift and Drag for Test 17

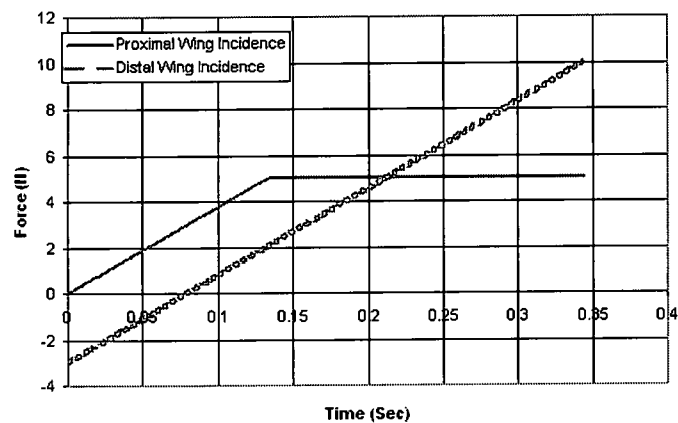
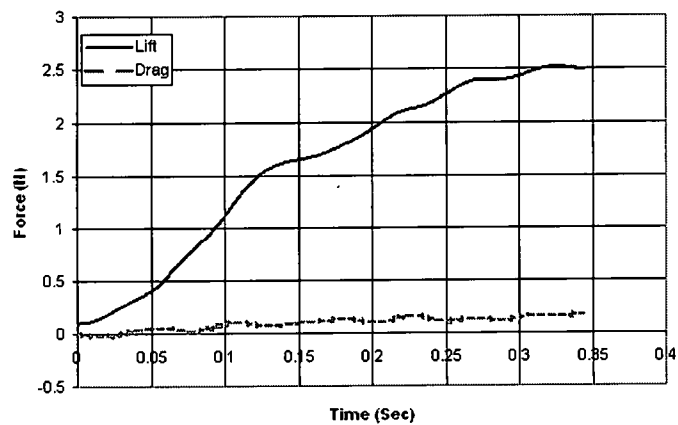


Figure C.2: Lift and Drag for Test 25

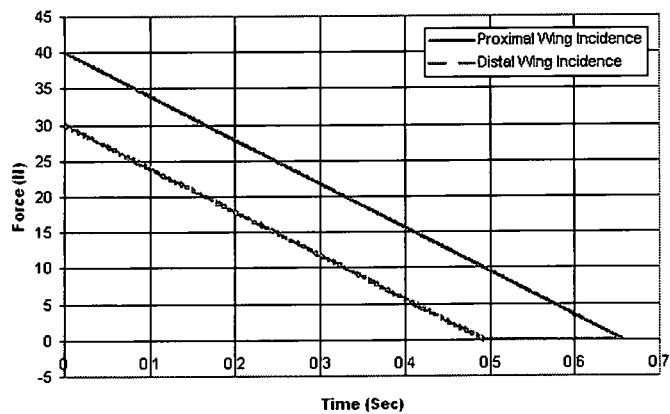
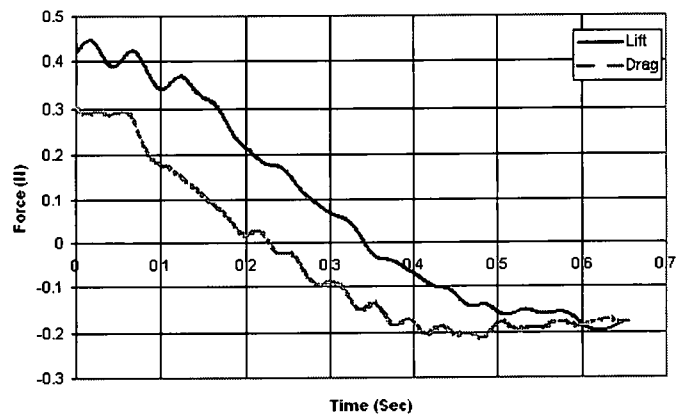


Figure C.3: Lift and Drag for Test 28

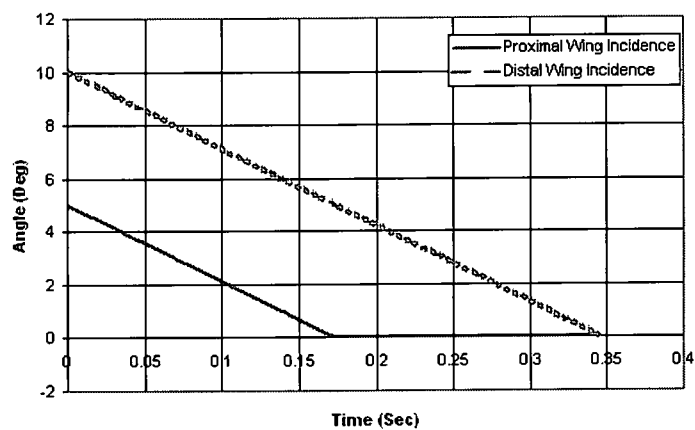
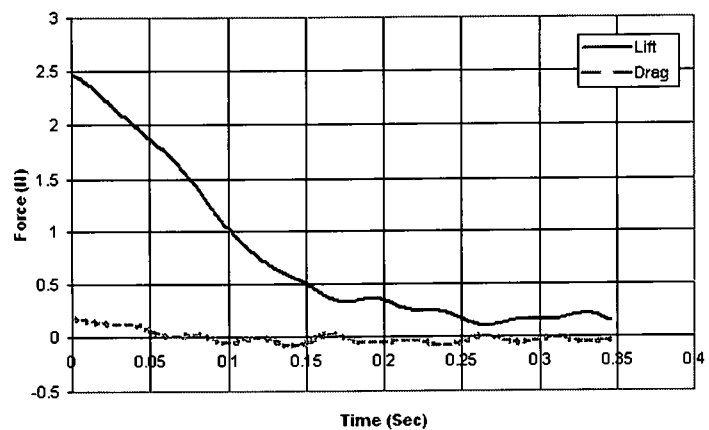


Figure C.4: Lift and Drag for Test 32

from around 40 degrees to 0 degrees and the distal wing sections moved from around 30 degrees to 0 degrees.

In test 32, results shown in Figure C.4, the wind tunnel speed was set to approximately 10 m/s and all the wing panels were programmed to start at 10 degrees and rotate to 0 degrees. Photographs taken during the test show that the proximal panels actually started at around 5 degrees and decreased to zero and the distal panels started around 10 degrees and rotated to 0 degrees as programmed.

Appendix D

Analysis Results

Several other tests were analyzed in IAMMS besides those described in this paper. The results for the additional runs are provided in this section.

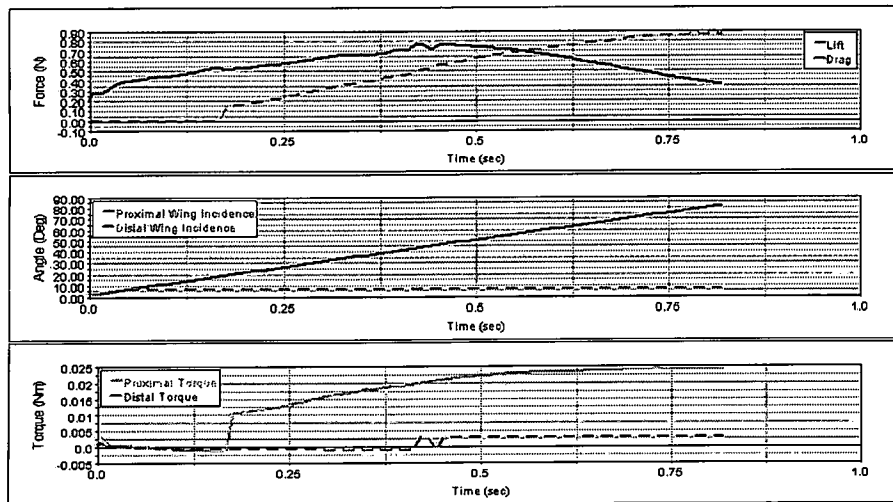


Figure D.1: Analytical Lift, Drag, and Pitching Moment Results for Test 15

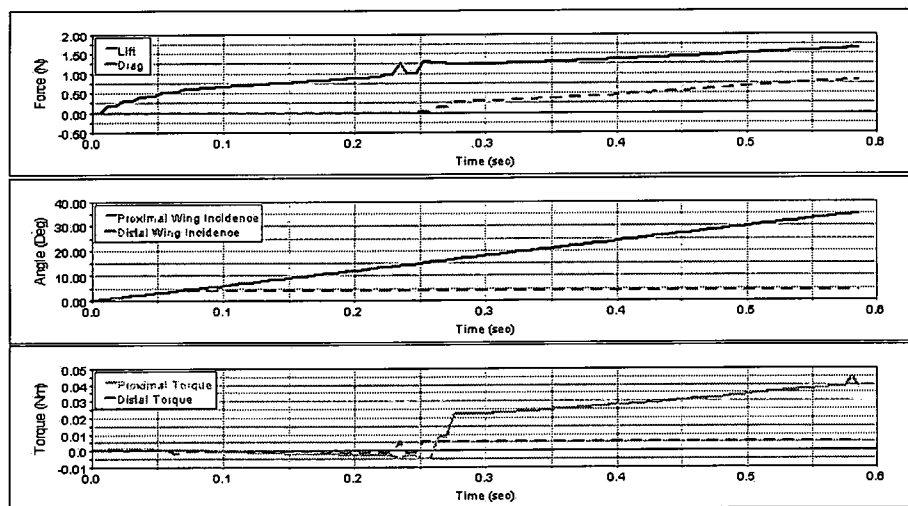


Figure D.2: Analytical Lift, Drag, and Pitching Moment Results for Test 20

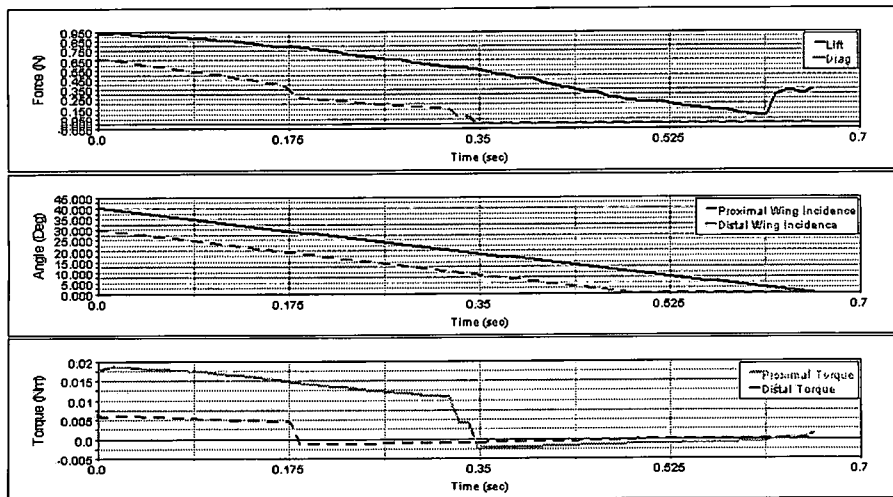


Figure D.3: Analytical Lift, Drag, and Pitching Moment Results for Test 28

Bibliography

- [1] Lee, D. N., Davies, M. N. O., Green, P. R., and Weel, R. T. R. V. D., "Visual Control of Velocity of Approach by Pigeons When Landing," Journal of Experimental Biology, 1993.
- [2] Keennon, M. and Grasmeyer, J., "Development of the Black Widow and Microbat MAVs and a Vision of the Future of MAV Design," AIAA International Air and Space Symposium and Exposition: The Next 100 Y, Dayton, Ohio, July 2003.
- [3] Raney, D. and Slominski, E., "Mechanization and Control Concepts for Biologically Inspired Micro Air Vehicles," Journal of Aircraft, Vol. 41, No. 6, December 2004.
- [4] Stewart, K., Wagener, J., Abate, G., and Salichon, M., "Design of the Air Force Research Laboratory Micro Aerial Vehicle Research Configuration," AIAA Aerospace Sciences Meeting and Exhibit, Reno, Nevada, January 2007.
- [5] Abdulrahim, M. and Lind, R., "Control and Simulation of a Multi-Role Morphing Micro Air-Vehicle," American Institute of Aeronautics and Astronautics, in review.
- [6] Grant, D., Abdulrahim, M., and Lind, R., "Flight Dynamics of a Morphing Aircraft Utilizing Independent Multiple-Joint Wing Sweep," AIAA Atmospheric Flight Mechanics Conference and Exhibit, Keystone, Colorado, August 2006.
- [7] Sheldahl, R. and Klimas, P., "Aerodynamic Characteristics of Seven Symmetrical Airfoil Sections Through 180-Degree Angle of Attack for Use in Aerodynamic Analysis of Vertical Axis Wind Turbines," Tech. rep., Sandia National Laboratories, Albuquerque, New Mexico, March 1981.
- [8] Pines, D. J. and Bohorquez, F., "Challenges Facing Future Micro-Air-Vehicle Development," Journal of Aircraft, Vol. 43, No. 2, March-April 2006, pp. 290–305.
- [9] Mueller, T. and DeLaurier, J., "Aerodynamics of Small Vehicles," Annual Reivew Fluid Mechanics, 2003.
- [10] Mueller, T. J., Kellogg, J. C., Ifju, P. G., and Shkarayev, S. V., Introduction to the Design of Fixed-Wing Micro Air Vehicles, American Institute of Aeronautics and Astronautics, Inc., 2006.

- [11] Mueller, T. and DeLaurier, J., "An Overview of Micro Air Vehicle Aerodynamics," Fixed and Flapping Wing Aerodynamics for Micro Air Vehicle Applications, edited by T. Mueller, Vol. 195, chap. 1, American Institute of Aeronautics and Astronautics, Reston, Virginia, 2001, pp. 1–10.
- [12] Broeren, A. P. and Bragg, M. B., "Unsteady Stalling Characteristics of Thin Airfoils At Low Reynolds Numbers," Fixed and Flapping Wing Aerodynamics for Micro Air Vehicle Applications, edited by T. Mueller, Vol. 195, chap. 1, American Institute of Aeronautics and Astronautics, Reston, Virginia, 2001, pp. 191–213.
- [13] Galbraith, M. C. and Visbal, M. R., "Implicit Large Eddy Simulation of Low Reynolds Number Flow Past the SD7003 Airfoil," 46th AIAA Aerospace Sciences Meeting and Exhibit, Reno, Nevada, January 2008.
- [14] Mueller, T. J., Kellogg, J. C., Ifju, P. G., and Shkarayev, S. V., Introduction to the Design of Fixed-Wing Micro Air Vehicles, American Institute of Aeronautics and Astronautics, Inc., 2006.
- [15] Abdulrahim, M. and Lind, R., "Using Avian Morphology To Enhance Aircraft Maneuverability," AIAA Atmospheric Flight Mechanics Conference and Exhibit, Keystone, Colorado, August 2006.
- [16] Magoteaux, K., Investigation of an Energy Harvesting Small Unmanned Air Vehicle, Master's thesis, University of Dayton, 2007.
- [17] Crowther, W., "Perched Landing and Takeoff for Fixed Wing UAVs," Applied Vehicle Technology Symposium, Ankara, October 2000.
- [18] Madangopal, R., Khan, Z., and Agrawal, S., "Biologically Inspired Design of Small Flapping Wing Air Vehicles Using Four-Bar Mechanisms And Quasi-steady Aerodynamics," Journal of Mechanical Design, Vol. 127, July 2005.
- [19] Moschetta, J.-M., Bataille, B., Thipyopas, C., and Shkarayev, S., "On Fixed-Wing Micro-Air Vehicles with Hovering Capabilities," 46th AIAA Aerospace Sciences Meeting and Exhibit, Reno, Nevada, January 2008.
- [20] Wickenheiser, A., Garcia, E., and Waszak, M., "Longitudinal Dynamics of a Perching Aircraft Concept," Vol. 5764, SPIE, Bellingham, Washington, 2005.
- [21] Azuma, A., The Biokinetics of Flying and Swimming, American Institute of Aeronautics and Astronautics, Reston, Virginia, 2nd ed., 2006.
- [22] Wu, J. and Popovic, Z., "Realistic Modeling of Bird Flight Animations," ACM Transactions on Graphics, 2003.
- [23] Tennekes, H., The Simple Science of Flight, From Insects to Jumbo Jets, MIT Press, Cambridge, Massachusetts, 1998.
- [24] Dial, K., "Avian Forelimb Muscles and Nonsteady Flight: Can Birds Fly Without Using the Muscles in Their Wings?" The Auk, 1992.

- [25] Liu, T., "Comparative Scaling of Flapping-and Fixed-Wing Flyers," AIAA Journal, Vol. 44, No. 1, January 2006.
- [26] Pennycuik, C., "Wingbeat Frequency of Birds in Steady Cruising Flight: New Data and Improved Predictions," Journal of Experimental Biology, 1996.
- [27] Green, P. R. and Cheng, P., "Variation in Kinematics and Dynamics of the Landing Flights of Pigeons on a Novel Perch," Journal of Experimental Biology, , No. 201, November 1998.
- [28] Tobalske, B. and Dial, K., "Flight Kinematics of Black-Billed Magpies and Pigeons Over a Wide Range of Speeds," Journal of Experimental Biology, 1996.
- [29] Withers, P., "An Aerodynamic Analysis of Bird Wings as Fixed Aerofoils," Journal of Experimental Biology, 1981.
- [30] Pennycuik, C., "A Wind-Tunnel Study of Gliding Flight in the Pigeon Columba Livia," Journal of Experimental Biology, 1968.
- [31] John D. Anderson, J., Fundamentals of Aerodynamics, Suzanne Jeans, 4th ed., 2007.
- [32] Sun, C. T., Mechanics of Aircraft Structures, John Wiley and Sons, Inc, 1998.
- [33] Ostowari, C. and Naik, D., "Post-Stall Wind Tunnel Data for NACA 44XX Series Airfoil Sections," Tech. rep., Solar Energy Research Institute, January 1985.
- [34] Beer, F. P., E. Russell Johnston, J., and DeWolf, J. T., Mechanics of Materials, McGraw-Hill, 3rd ed., 2002.
- [35] Daniel, I. and Ishai, O., Engineering Mechanics of Composite Materials, Oxford University Press, Oxford, New York, 2nd ed., 2006.
- [36] Huber, J., Fleck, N., and M.F.Ashby, "The Selection of Mechanical Actuators Based on Performance Indices," Proc. R. Soc. Lond., 1997.
- [37] Bell, D. J., Lu, T. J., Fleck, N. A., and Spearing, S. M., "MEMS actuators and sensors: Observations on their performance and selection for purpose," Journal of Micromechanics and Microengineering, 2005.
- [38] Wegst, U. G. K. and Ashby, M. F., "The mechanical efficiency of natural materials," Philosophical Magazine, Vol. 84, No. 21, 2004.
- [39] Barlow, J., William Rae, J., and Pope, A., Low-Speed Wing Tunnel Testing, John Wiley and Sons, New York, New York, 3rd ed., 1999.
- [40] Brandon, J. M., "Dynamic Stall Effects and Applications to High Performance Aircraft," 2003.
- [41] Reich, G. W., Bowman, J. C., Sanders, B., and Frank, G. J., "Development of and Integrated Aeroelastic Multibody Morphing Simulation Tool," AIAA 47th Structures Structural Dynamics, and Materials Conference, Newport, Rhode Island, May 2006.

R00 2593726